DOT/FAA/AR-00/33

Office of Aviation Research
Washington, D.C. 20591

Field Verification of a 3D Finite Element Rigid Airport Pavement Model

July 2000

Final Report

This document is available to the U.S. public through the National Technical Information Service (NTIS), Springfield, Virginia 22161.

U.S. Department of Transportation
Federal Aviation Administration

NOTICE

Technical Report Documentation Page

1. Report No. DOT/FAA/AR-00/33	2. Government Accession No.	3. Recipient's Catalog No.

4. Title and Subtitle FIELD VERIFICATION OF A 3D FINITE ELEMENT RIGID AIRPORT PAVEMENT MODEL	5. Report Date July 2000 6. Performing Organization Code
7. Author(s) David R. Brill	8. Performing Organization Report No.
9. Performing Organization Name and Address Galaxy Scientific Corporation 2500 English Creek Ave., Bldg. C Egg Harbor Twp., NJ 08234-5562	10. Work Unit No. (TRAIS) 11. Contract or Grant No. DTFA030-95-D-00019
12. Sponsoring Agency Name and Address U.S. Department of Transportation Federal Aviation Administration Office of Aviation Research Washington, DC 20591	13. Type of Report and Period Covered Final Report 14. Sponsoring Agency Code AAS-200

15. Supplementary Notes

The Federal Aviation Administration William J. Hughes Technical Center COTR was Dr. Satish K. Agrawal

16. Abstract

Field data from the Federal Aviation Administration (FAA) Runway Instrumentation Project at Denver International Airport, Colorado, were analyzed and compared to three-dimensional finite element model predictions. Data collected at the Denver test site included strains and deflections of the rigid pavement structure under typical in-service aircraft loads. A statistical analysis of the sensor data yielded mean values of key responses such as peak strain, peak deflection, and load transfer efficiency at transverse joints, which were then compared to results of the finite element analysis. The comparisons reported herein indicate overall good agreement between measured and predicted responses.

17. Key Words Three-dimensional finite element method, Pavement instrumentation, Airport pavement response, Pavement modeling, Load transfer efficiency	18. Distribution Statement Document is available to the public through the National Technical Information Service (NTIS) Springfield, Virginia 22161.

19. Security Classif. (of this report) Unclassified	20. Security Classif. (of this page) Unclassified	21. No. of Pages	22. Price

Form DOT F1700.7 (8-72) Reproduction of completed page authorized

ACKNOWLEDGEMENTS

The work described in this report was performed for the U.S. Department of Transportation, Federal Aviation Administration (FAA), Airport Technology R&D Branch, under Contract DTFA030-95-D-00019. Dr. Satish K. Agrawal is Manager of the Airport Technology R&D Branch.

The contributions of the following individuals are acknowledged: Mr. Charles Teubert, Dr. Edward H. Guo, Ms. May Dong, Dr. Yingwu Fang, and Dr. Gordon F. Hayhoe.

TABLE OF CONTENTS

Preceding Page Blank

LIST OF FIGURES

LIST OF TABLES

EXECUTIVE SUMMARY

A three-dimensional finite element model of a rigid airport pavement developed by the Federal Aviation Administration (FAA) predicts the response of the rigid pavement to aircraft gear loads. Responses predicted by the finite element model include stresses and strains in the concrete slab and the deflected shape of the pavement structure. These responses were verified by comparison with field data collected over an approximately 20-month period at the FAA Runway Instrumentation Project located at Denver International Airport, Colorado. The loading aircraft at the Denver site included B-727, B-737, B-757, DC-10, and B-777 aircraft types. Statistical analyses were performed on the field-collected data to provide mean values of variables such as peak strain and deflection that were then compared to the deterministic response provided by the finite element model for the same landing gear configurations.

Comparisons between field-measured data and finite element model predictions of strain and deflection are presented in this report. These comparisons indicate generally good agreement between the three-dimensional finite element model and mean values of peak strain and peak deflection measured at the Denver site. Statistical analysis verifies that peak deflection readings at slab edges are more affected by seasonal temperature variations than those in the interior of the slab. It is also shown that the magnitudes of computed tensile strains in the concrete slabs are dependent on the level of bond assumed for the slab/base interface, and that an intermediate bond model (neither fully bonded nor fully unbonded) may come closest to predicting the level of strain observed in the field.

Similar comparisons are presented for load transfer efficiency at rigid pavement joints. Methods of estimating the in-service load transfer efficiency from analysis of pavement sensor records are presented. Load transfer efficiency may be either deflection-based or strain-based. The results presented in this report show significant seasonal variations due to temperature in both deflection-based and strain-based load transfer efficiency for transverse joints at the Denver test site. Because of this variation, it is important to consider whether finite element predictions of load transfer efficiency in joints are representative of winter or summer values.

Preceding Page Blank

INTRODUCTION

A three-dimensional (3D) finite element model of rigid pavement response to aircraft loading was developed by the Federal Aviation Administration (FAA). The development and computer implementation of the 3D finite element model is described in FAA Report DOT/FAA/AR-97/47, "Development of Advanced Computational Models for Airport Pavement Design" [1]. This report is a continuation of that report and covers comparison of the 3D finite element model predictions with field data.

Comparisons to field data obtained from the FAA Runway Instrumentation Project at Denver International Airport (DIA) [2, 3] are presented in detail. The 3D finite element model predicts peak strain and deflection responses for various aircraft types that are in very good agreement with the mean in-service values of these responses from runway instrumentation at DIA. The purpose of field comparisons was threefold:

- To compare numerical model predictions with insitu pavement responses;
- To use the 3D finite element model as an analytical tool for interpreting DIA instrumented runway data;
- To provide data for ongoing development of the 3D finite element model.

FAA RUNWAY INSTRUMENTATION PROJECT

The FAA Runway Instrumentation Project at DIA was the source of the field data used to field-verify the finite element model predictions. Sensors were installed in a portion of the runway pavement at DIA runway 34R-16L. The installed sensors are of two general types: (1) dynamic sensors and (2) static sensors. Dynamic sensors, including H-bar strain gauges, linear variable differential transformers (LVDTs), and position strain gauges are triggered by an aircraft event on the runway and record a dynamic signal related to the triggering event. Depending on the aircraft gear type and position, the dynamic signal may contain one or more peaks. Static sensors, including embedded temperature and moisture gauges, are not triggered by the passing aircraft. Rather, they record values at set intervals, generally every hour. The layout of the dynamic gauges at runway 34R-16L is shown in figures 1 and 2.

Data received from the instrumented runway is automatically processed and uploaded into a database. Each event triggering a dynamic response is assigned both a unique identifying number in the database and a date/time stamp that identifies when the event occurred in Julian time. Greenwich Mean Time (GMT) rather than local Denver time is used for the database. The aircraft type is identified from characteristics of the recorded signal and entered in the database. Events are classified as arrival or departure events. Where possible, the takeoff weights of departing aircraft are established by matching database events to the same events listed in airline flight schedules.

The entire database is accessible to the public via the Internet [2]. By using Structured Query Language (SQL) commands online, particular events or groups of related events can be retrieved from the database. Events in a query may be related by aircraft type, time of year, time of day, by a response at a specific sensor, or by combinations of these parameters. As shown in the

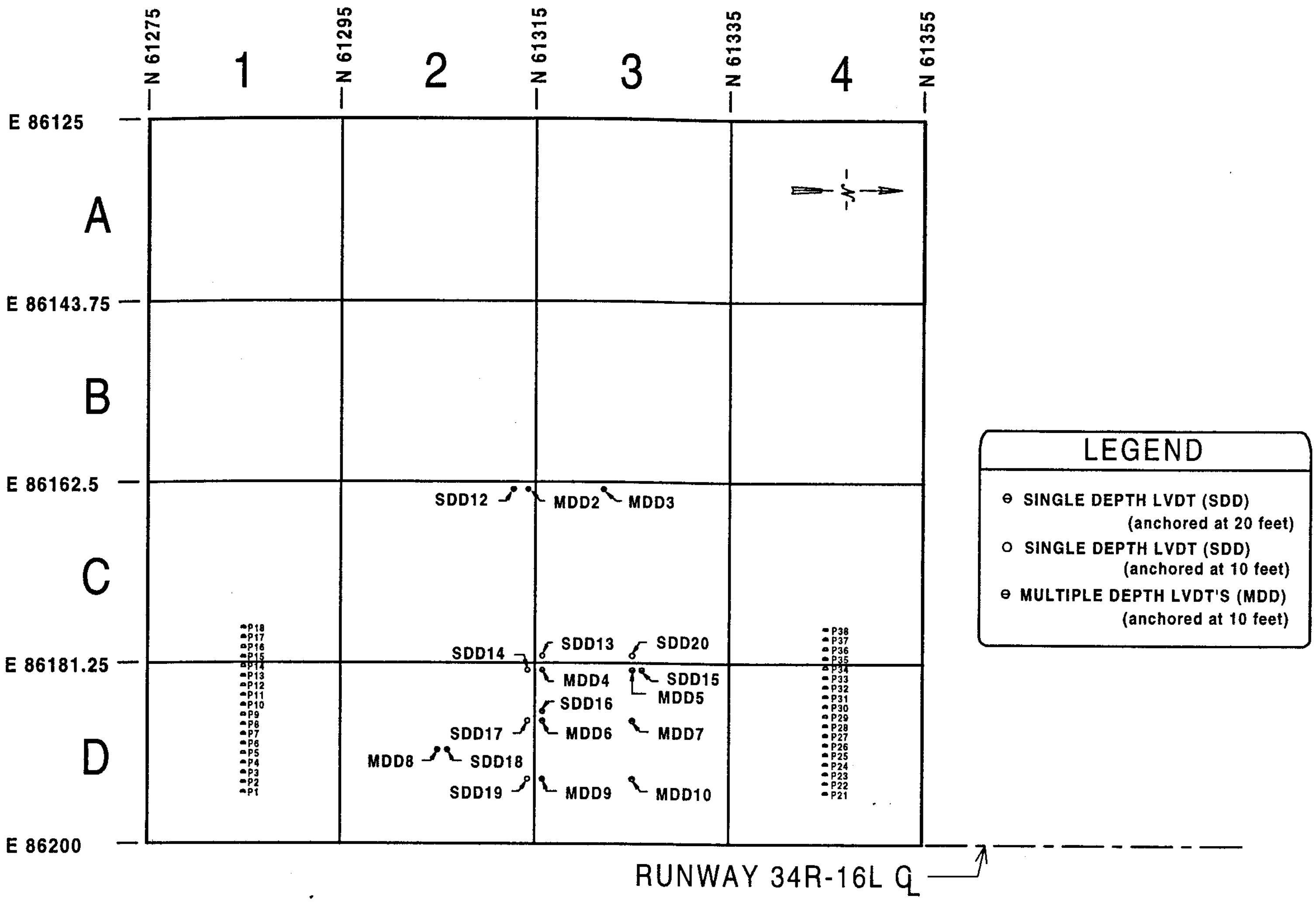

FIGURE 1. LOCATION OF LVDT SENSORS

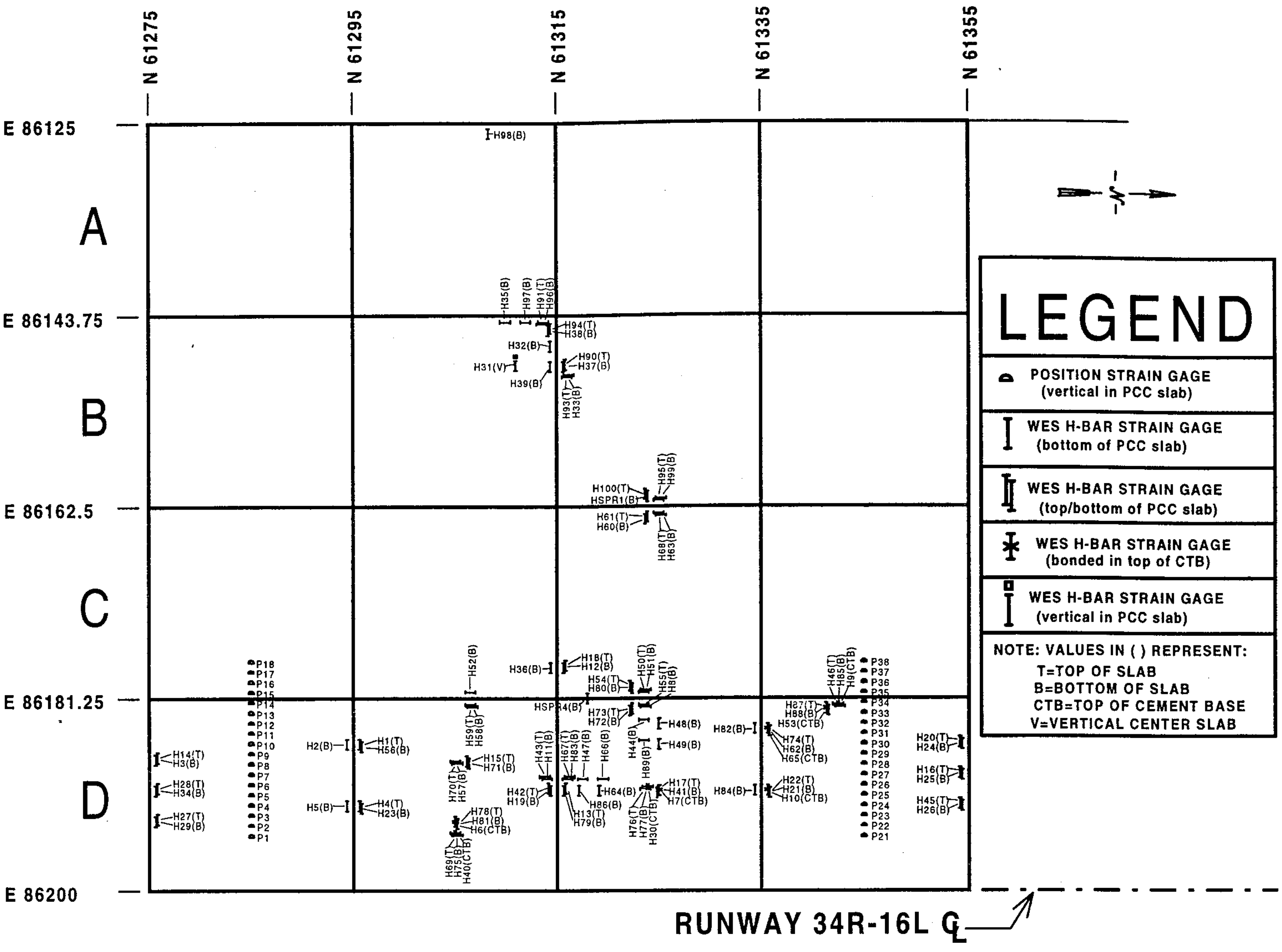

FIGURE 2. LOCATION OF H-BAR SENSORS

following sections, the online query feature is an important tool for data analysis and model verification.

METHOD OF STATISTICAL ANALYSIS

The 3D finite element model provides a unique deterministic solution to the problem of pavement loading for a particular combination of wheel loads and pavement properties. To verify this model, the simplest approach is to identify an event in the database for which the actual load conditions closely approximate the model assumptions and then to compare the finite element solution to the peak sensor readings for this event. This "single observation" approach assumes that any given reading is typical of all such readings for similar load conditions. However, a single measurement may not be an accurate reflection of the typical response to a load, due to variability in the sensor data. The advantage of a statistical approach is that it recognizes that variability in the data is unavoidable and gives it a mathematical expression. In the statistical approach, the deterministic solution from the finite element model is compared not to a single measurement, but to the mean of many measurements from similar events. Statistical tools also allow additional information to be extracted from the data. For example, the expected difference in peak stress due to seasonal changes in temperature.

Quantities measured by the pavement sensors, such as peak strains and deflections, are treated as random variables for the purpose of statistical analysis. Certain variables (aircraft type, aircraft gross weight, and time of year) are presumed to have a major, quantifiable effect on the measured response at a given gauge, so these variables are controlled explicitly in the analysis. Other variables may also have an effect, but either the effect is too minor to be quantified or else there is insufficient information available from the database or from other sources to establish a definite relationship. Factors that fall into the latter category include:

1. Sensitivity to daily temperature fluctuations.
2. Sensitivity to weather conditions including rainfall, ice, and humidity.
3. Uncertainty in tracking the position of the aircraft on the pavement.
4. Uncertainty in determining the total aircraft weight.
5. Variations in tire pressure and tire contact area.
6. Variations in the distribution of the aircraft weight among the landing gears and among the individual tires in the gear truck.
7. Influence of aircraft speed and acceleration.
8. Electronic noise and sampling errors in the sensor signals.

The set of all peak readings of a particular sensor for a given time period and a given aircraft type constitutes the initial data set for analysis. Since the initial data set obtained by querying the database may include spurious, duplicate, or other unwanted data (such as peak readings for events where the aircraft wheel passed either to the right or to the left of the sensor), additional tests are generally needed to eliminate these unwanted events from the data set. These tests may include restrictions applied to the position sensor data. The data set is further restricted by eliminating all those events for which the gross weight of the loading aircraft is not entered in the database. The remaining data are then adjusted to account for variations in the aircraft gross weight. The following adjustment factor assumes that a linear relationship exists between the gross weight of the aircraft and the magnitude of the peak response:

$$f = \frac{w_{FEA}}{w_g} \tag{1}$$

In equation 1, w_{FEA} is the aircraft weight assumed in the finite element analysis for the aircraft type and w_g is the aircraft gross weight from the database for a particular event. Multiplying all the peak values in the data set by the adjustment factor f has the effect of putting all the responses in the data set on a common weight basis.

The sample mean, sample variance, and other statistics are calculated for the weight-adjusted data using the standard mathematical formulas available in statistics textbooks. For purposes of statistical analysis, the values in the adjusted data set are treated as though randomly sampled from a normally distributed population with mean μ and variance σ^2. Here, the unknown population mean μ is understood as the mean that would be obtained from analyzing a very large number of hypothetical events involving the same aircraft loading, under the same general conditions, as the actual events in the sample. From the statistical law of averages, it follows that the sample mean $\bar{x}$ is an estimate of the "true," or population, mean μ. Moreover, for any sample size n, the 95% confidence limits for the true mean are expressed mathematically by

$$P\left(\bar{x} - t_{n-1}(0.025)\frac{s}{\sqrt{n}} < \mu < \bar{x} + t_{n-1}(0.025)\frac{s}{\sqrt{n}} \right) = 0.95 \tag{2}$$

where s is the sample variance and $t_{n-1}(0.025)$ refers to points of Student's t-distribution for $n-1$ degrees of freedom.

FINITE ELEMENT MODEL OF RUNWAY 34R-16L

Figure 3 shows the pavement structure used to represent runway 34R-16L in the 3D finite element model. The structural properties of the various material layers are based on a combination of laboratory test results and heavy weight deflectometer (HWD) analysis of the as-built pavement. The properties used and their sources are listed in table 1.

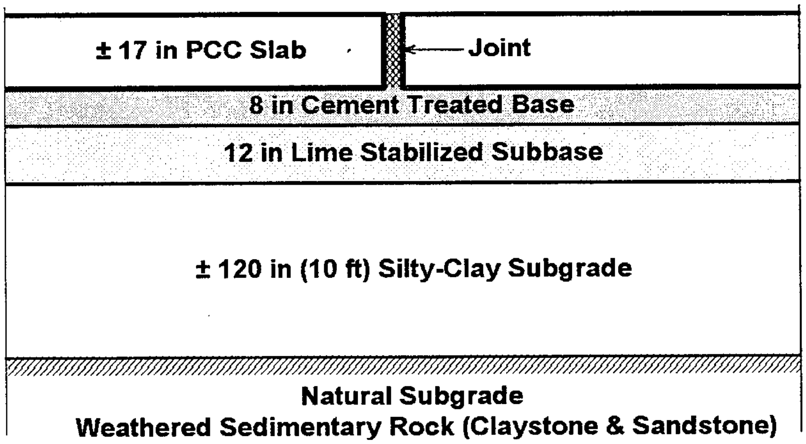

FIGURE 3. CROSS SECTION OF DIA RUNWAY 34

TABLE 1. LAYER PROPERTIES FOR FINITE ELEMENT ANALYSIS

Layer	*E*, psi	Poisson's Ratio	Source (i.e., lab or field test)
Concrete slab	4,410,000	0.22	6″ concrete core sample in lab
CTB	1,200,000	0.20 (assumed)	Heavy-weight deflectometer (HWD)
Lime subbase	440,000	0.25 (assumed)	Heavy-weight deflectometer (HWD)
Subgrade (fill)	15,000	0.40 (assumed)	Resilient modulus (M_R) test
Subgrade (natural)	rigid	N.A.	N.A.

The nominal thickness of the portland cement concrete (PCC) layer is 17 inches (43.2 cm). However, the as-built thickness varies from location to location throughout the 16-slab test area. The minimum measured PCC thickness is 16.7 inches (42.4 cm) near gauge H20, and the maximum measured PCC thickness is 18.8 inches (47.8 cm) near H36. Therefore, the actual thickness of the concrete at the location of the gauge being studied was used for finite element computations.

The subgrade in the vicinity of the test section on runway 34R-16L consists of 5 to 10 feet (1.52 to 3.05 m) of silty-clay fill overlaying the natural subgrade material at the site. In the Preliminary Pavement Design Report for DIA [4], the subgrade fill material is designated as "Zone A Material" and is characterized as a sandy, "relatively select" clay with a recommended k value of 150 pci (40.7 kg/cm^3) untreated and a California Bearing Ratio (CBR) of 4.5. The Young's modulus value E = 15,000 psi (103.5 MPa) used for this material in finite element analyses is based on laboratory measurement of the resilient modulus (E_R). The natural subgrade material below the replacement fill is characterized in the pavement engineer's report as "severely weathered and comparatively unweathered sedimentary bedrock, which is a portion of the Denver Formation." Based on the information contained in the pavement engineer's report, it was felt that assuming a 10-foot depth of clay subgrade material overlaying rigid material would be representative of the actual conditions at the test site.

The use of a relatively thin subgrade overlaying a rigid base (figure 3) is a departure from the previously developed 3D rigid pavement model [3], which uses a deep subgrade layer to approximate infinite subgrade conditions. When "infinite subgrade" conditions were assumed in the present case, it was found that the 3D finite element model predicted unrealistically high surface deflections, several times higher than the largest recorded values at DIA. It was felt that for model verification purposes, the model assumptions should be allowed to reflect, as accurately as possible, the actual conditions prevailing at the test site, including a relatively shallow subgrade. An exploded perspective view of the 3D finite element mesh used for computations is shown in figure 4.

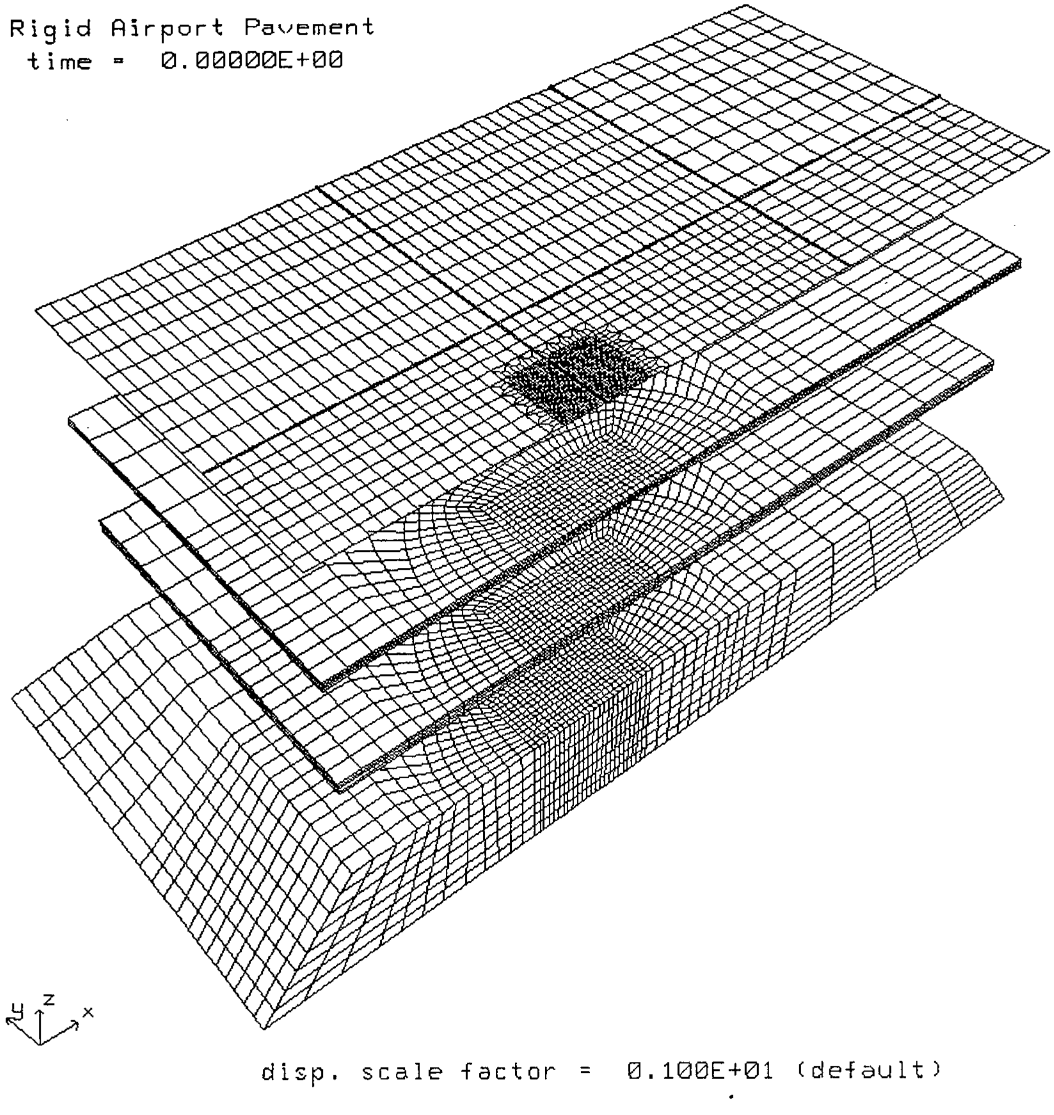

FIGURE 4. 3D MESH FOR FINITE ELEMENT COMPUTATIONS

PEAK STRAIN COMPARISONS

Dynamic strains in runway 34R-16L are measured by 101 H-bar (HB) strain gauges placed at various locations in the PCC and cement-treated base (CTB) layers. Figure 1 shows the location and orientation of the H-bar strain gauges. Most gauges are positioned near the top (T) or bottom (B) of the PCC slab.

For any given aircraft event, only a relatively small subset of strain gauges records usable strain data. The strain gauges that record data for an event are those located on or near the wheel path. Strain gauges located a short distance away from the wheel path produce only a flat line or noise. Thus, in many cases a reasonable approximation of the aircraft path can be obtained from analyzing the H-bar strain gauge data alone. However, a more accurate means of determining the aircraft path is from the 36-position strain gauge (P) sensors installed in the runway. The position strain gauges are evenly spaced at one-foot intervals in two east-west rows, as shown in figure 1. An aircraft wheel passing over a position sensor produces a sharp peak in the response of the P sensor in the path, while the response of the adjacent P sensors to the same event is usually much smaller and less distinct. By analyzing the response of position sensors for an event, the lateral position of the aircraft wheels as the gear crosses the sensor banks can be established to an accuracy of a few inches. The lateral position of the aircraft gears at any point within the test area can then be estimated by linear interpolation between the two rows of position sensors.

For each aircraft event, the database stores complete data records from up to 10 H-bar gauges. The peak strain value is calculated by filtering the signal, finding the minimum and maximum values in the filtered signal record, finding "left offset" (if not enough points on left, compute right offset) by computing the average value of the filtered signal, and subtracting the left (or right) offset from minimum or maximum value (whichever has been selected). Peak strain data is stored in tables whose names are the same as the sensor designations. Within the sensor tables, each peak strain entry is associated with the unique event number of the aircraft event that created it. For example, if aircraft event number 103 caused a peak strain to be recorded at strain gauge H42, then the value of that peak strain is stored along with the identifying number "103" in a table called *hb42*. Although each strain gauge may record multiple peak values for a single event (with the number of peaks recorded generally corresponding to the number of axles in the landing gear of the aircraft that caused the event), only the largest peak value is currently stored in the database. An example of a complete H-bar strain gauge record for a B-777 event, containing three distinct peaks, is shown in figure 5.

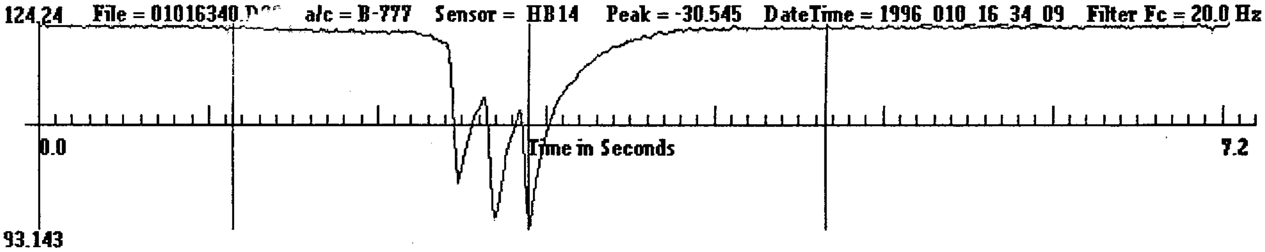

FIGURE 5. DYNAMIC STRAIN RECORD FROM H14 (B-777 DEPARTURE)

Position sensor peak data are stored in tables labeled P1, P2, P3, etc., in the same manner as the H-bar gauge peak data.

Sets of comparable peak strains corresponding to certain aircraft types were selected from the sensor tables by querying the online database. All database queries use the SQL syntax. A typical SQL instruction is as follows:

```
select aircraft.event#, datetime, aircraftweight, hb42.peak1
from aircraft, hb42, p5, p26
where aircrafttype = 'B-727-200'
and aircraft.event# = hb42.event#
and aircraft event# = p5.event# and aircraft.event# = p26.event#
and aircraftweight > 0
and datetime between 19960010001 and 19960602400;
```

The first line of the above query specifies which data will be retrieved from the database. The requested fields are the internal database event number (*event #*), the date/time stamp for the event (*datetime*), the gross takeoff weight of the departing aircraft (*aircraftweight*), and the value of peak strain at the sensor under consideration, in this case H-bar sensor H42 (*hb42.peak1*).

The second line of the query specifies which tables in the database contain the data to be used in carrying out the instruction. Table *aircraft* contains the date/time, aircraft type, and aircraft gross weight data for the event. Tables *hb42, p5,* and *p26* contain peak values for the respective sensors, as discussed above. The *event#* field is contained in all tables and is used in the database to relate data fields for the same event stored in different tables.

The third line restricts the database search to events where the aircraft type is identified in the database as a B-727-200 aircraft.

The fourth line restricts the database search to only events that produced a peak response at H42. This includes events that covered the gauge and events where the wheel passed near the gauge but did not cover it.

The fifth line further restricts the search to events that produced a peak response at both position sensors P5 and P26. This restriction is useful for eliminating events where the wheel passed close enough to H42 to produce a response (line 4), but where the tire footprint did not actually cover the gauge. From figure 1, it can be inferred that if an event triggers a response at both P5 and P26, then there is a high probability that H42 is covered by an aircraft tire during that event. (This assumes that the same aircraft tire triggers both position sensors and that the wheel path between position sensors is approximately a straight line. A manual check of the events is necessary to verify that the same wheel in fact triggered both position sensors.) A similar query could be made using peak responses at position sensors P6 and P25, and the results combined to give the set of all B-727-200 events covering H42 (subject to manual verification).

The sixth line has the effect of restricting the query to events for which the gross weight of the loading aircraft is known from airline schedules. (For events where the gross weight is unknown, the *aircraft weight* field contains the value 0 (zero)).

The last line restricts the search to events that occurred between December 1, 1995 and February 29, 1996. The date and time are given in Julian time format. It should also be noted that event times stored in the database are in GMT, which is converted to Mountain Standard Time by subtracting 7 hours.

INTERIOR LOADS.

Computed strains for interior loading were compared to peak strain values recorded by three H-bar strain gauges located in the interior of slab D-2. The strain gauges used for the comparison were H15, H70, and H71 (figure 1). A fourth H-bar sensor at the same location, H57, was not used for the comparison because it failed to perform during the time period of interest (January 1996 to August 1997). As shown in figure 1, sensors H15 and H71 are oriented in the transverse (east-west) direction, while H70 is oriented in the longitudinal (north-south) direction. Sensors H15 and H70 are located near the top surface of the PCC slab, while H71 is located near the slab bottom, close to the interface with the CTB layer.

The following five aircraft types were used for comparisons: B-727, B-737, B-757, DC-10, and B-777. For each aircraft category, the set of events used to compute the mean and range values was the set of all events in the database as of August 1997 for which

- the gross aircraft weight was known from airline schedules, and
- analysis of the position sensor responses indicated that one of the aircraft tires in the gear assembly covered the recording H-bar gauge.

For a dual-wheel gear, either the left tire or the right tire in the assembly may cover the recording gauge, as shown in figure 6. The analysis did not make any distinction between the responses for the two cases.

The number of events contained in each aircraft data set based on the above criteria ranged from a low of one for the B-777 airplane to a high of 66 for the B-737. The higher number of events in the B-737 and B-727 categories reflects the higher aircraft traffic for those models.

Tables 2 through 4 present a statistical summary of the strain gauge data used for the comparisons. For each aircraft data set, the peak strain readings recorded at the gauge were adjusted to a uniform weight basis using the factor in equation 1. As explained above, the value of w_{FEA} is the gross aircraft weight used in the finite element analysis. The 95% confidence limits for the mean were calculated using equation 2. The 95% confidence limits were computed for the B-727, B-737, and B-757 means only. The 95% confidence limits for the mean were not computed for the DC-10 and B-777 aircraft types, because of the small number of events involving those aircraft types. At least six events were required to compute meaningful statistics.

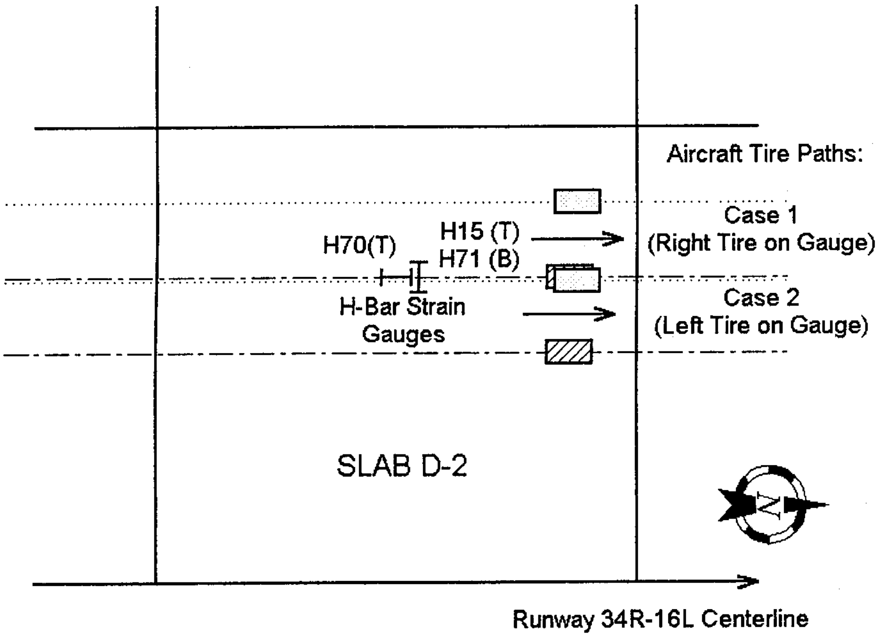

FIGURE 6. H-BAR STRAIN GAUGE COVERAGE FOR INTERIOR LOAD CASE

TABLE 2. SUMMARY STATISTICS FOR PEAK STRAIN AT H15

Aircraft Type	Count (n)	Aircraft Wt., lbs.		Adjusted Peak Strain (10^{-6})			95% Confidence Limits for Mean (±)
		avg. w_g	w_{FEA}	Mean	Range	Variance (10^{-12})	
B-727	30	158,982	172,000	-17.95	11.03	7.58	1.03
B-737	66	108,358	100,000	-11.63	7.93	3.92	0.47
B-757	18	188,571	250,000	-22.25	8.00	4.92	1.10
DC-10	5	354,569	458,000	-32.58	7.54	11.88	-
B-777	1	428,351	634,500	-27.69	-	-	-

10^{-6} signifies microstrain. Variance is microstrain squared.

TABLE 3. SUMMARY STATISTICS FOR PEAK STRAIN AT H70

Aircraft Type	Count (n)	Aircraft Wt., lbs.		Adjusted Peak Strain (10^{-6})			95% Confidence Limits for Mean (±)
		avg. w_g	w_{FEA}	Mean	Range	Variance (10^{-12})	
B-727	30	158,982	172,000	-24.81	8.84	5.31	0.86
B-737	66	108,358	100,000	-16.24	8.84	3.31	0.45
B-757	18	188,571	250,000	-22.48	6.19	3.29	0.90
DC-10	5	354,569	458,000	-30.18	4.01	2.42	-
B-777	1	428,351	634,500	-24.10	-	-	-

TABLE 4. SUMMARY STATISTICS FOR PEAK STRAIN AT H71

Aircraft Type	Count (n)	Aircraft Wt., lbs.		Adjusted Peak Strain (10^{-6})			95% Confidence Limits for Mean (±)
		avg. w_g	w_{FEA}	Mean	Range	Variance (10^{-12})	
B-727	30	158,982	172,000	14.16	10.02	6.35	0.94
B-737	66	108,358	100,000	8.54	7.16	3.18	0.30
B-757	18	188,571	250,000	14.38	7.23	3.84	1.10
DC-10	5	354,569	458,000	23.23	8.75	3.16	-
B-777	1	428,351	634,500	18.66	-	-	-

Results of the 3D finite element analysis for interior aircraft loading are summarized in table 5. Computed strains are reported for three slab locations, corresponding to the locations of the three H-bar gauges, as follows:

1. Strain A is the maximum transverse strain under the tire at the vertical location corresponding to the installed depth of H15 (3.61 inches (9.2 cm) below the top surface of the slab).

2. Strain B is the maximum longitudinal strain under the tire at the vertical location corresponding to the installed depth of H70 (3.58 inches (9.1 cm) below the top surface of the slab).

3. Strain C is the maximum transverse strain under the tire at the vertical location corresponding to the installed depth of H71 (16.98 inches (43.1 cm) below the top surface of the slab).

TABLE 5. COMPUTED STRAINS FOR INTERIOR STRAIN COMPARISON

Aircraft Type	3D Finite Element Computed Strain (10^{-6})					
	Sliding Interface Model			Tied Interface Model		
	Strain A	Strain B	Strain C	Strain A	Strain B	Strain C
B-727	-19.05	-23.70	28.24	-15.98	-19.07	13.91
B-737	-12.25	-14.91	18.17	-10.24	-12.26	9.23
B-757	-21.60	-19.74	32.05	-18.24	-16.89	15.44
DC-10	-29.02	-26.52	43.05	-25.39	-23.50	21.69
B-777	-28.29	-25.45	39.99	-23.98	-24.13	25.02

Strains were computed assuming a PCC slab thickness equal to the actual slab depth measured at the H-bar location. The concrete thickness used for the Strain A, Strain B, and Strain C computations were 17.89 inches (45.44 cm), 17.98 inches (45.67), and 17.89 inches (45.44 cm) respectively (representing the measured concrete thickness at H15, H70, and H71 respectively). The material properties in table 1 were used for all finite element computations. Two values of computed strain are reported for each aircraft type at each location. The first value (sliding interface) is based on the usual model assumption of a full sliding interface between the bottom of the concrete slab and the top of the CTB. The second value (tied interface) instead assumes full bonding at the slab/base interface. The two models are identical in all other respects. These two cases provide an upper and lower bound for the partial bonding case.

Figures 7 through 9 compare the measured peak strain data from tables 2 through 4 to the finite element strain values from table 5. These figures demonstrate that for strains in the interior of the slab, the tied interface finite element model (assuming complete bonding between the slab and the base) yields better overall agreement with DIA data than the sliding interface model (assuming zero bonding) for strains measured at the top of the slab. The reverse was observed for strains at the bottom of the slab.

1. Zero bond (sliding interface model): When zero bond is assumed between the slab and base layers, the result is that computed compressive strains A and B (top of slab) agree very well with the corresponding mean strains at H15 and H70, but the computed tensile strain C (bottom of slab) is approximately twice as large as the corresponding mean strain at H71 and well out of the range of observed values.

2. Full bond (tied interface model): With full bond, the computed strains at the bottom of the slab show remarkably good agreement with the field data. Specifically, the computed value of tensile strain C is within the calculated 95% confidence limits for the mean of peak strain at H71, for the three aircraft types B-727, B-737, and B-757. The top-of-slab strain comparisons are less favorable than for the zero bond model, but still reasonable.

The results shown in figures 7 through 9 strongly suggest that significant bonding does develop at the center of the slab, notwithstanding the presence of a bond breaker. In this case, the finite element model assuming full bonding predicts the measured critical pavement response much better than the model assuming no bonding.

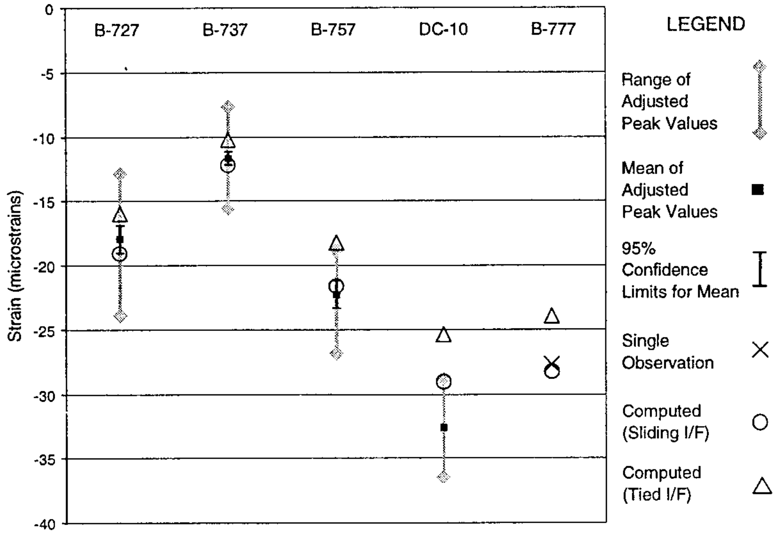

FIGURE 7. PEAK STRAIN RESPONSE AT STRAIN GAUGE H15 COMPARED TO 3D FINITE ELEMENT SOLUTION FOR VARIOUS AIRCRAFT TYPES

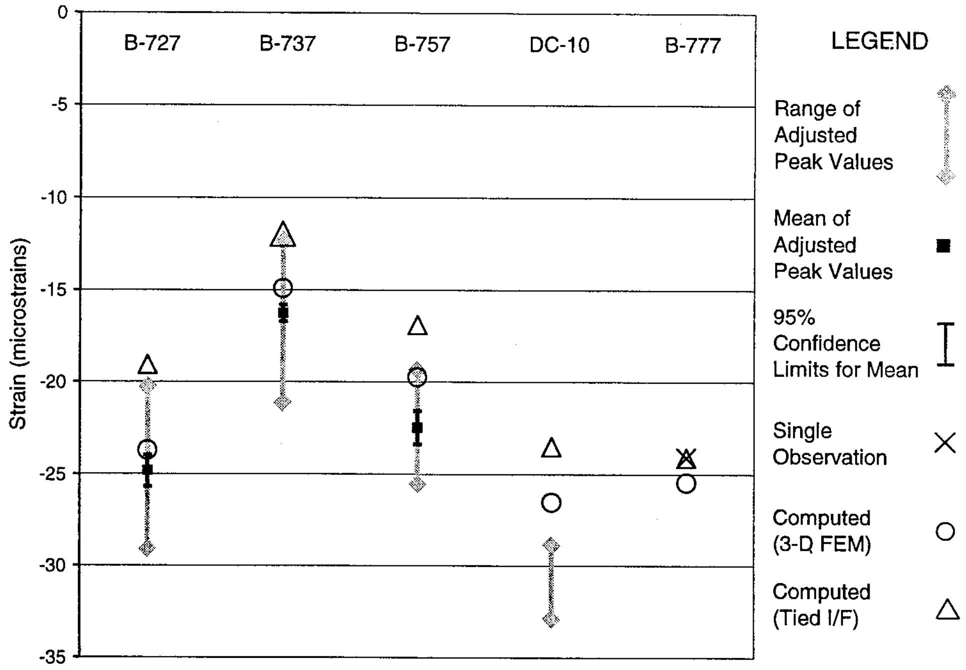

FIGURE 8. PEAK STRAIN RESPONSE AT STRAIN GAUGE H70 COMPARED TO 3D FINITE ELEMENT SOLUTION FOR VARIOUS AIRCRAFT TYPES

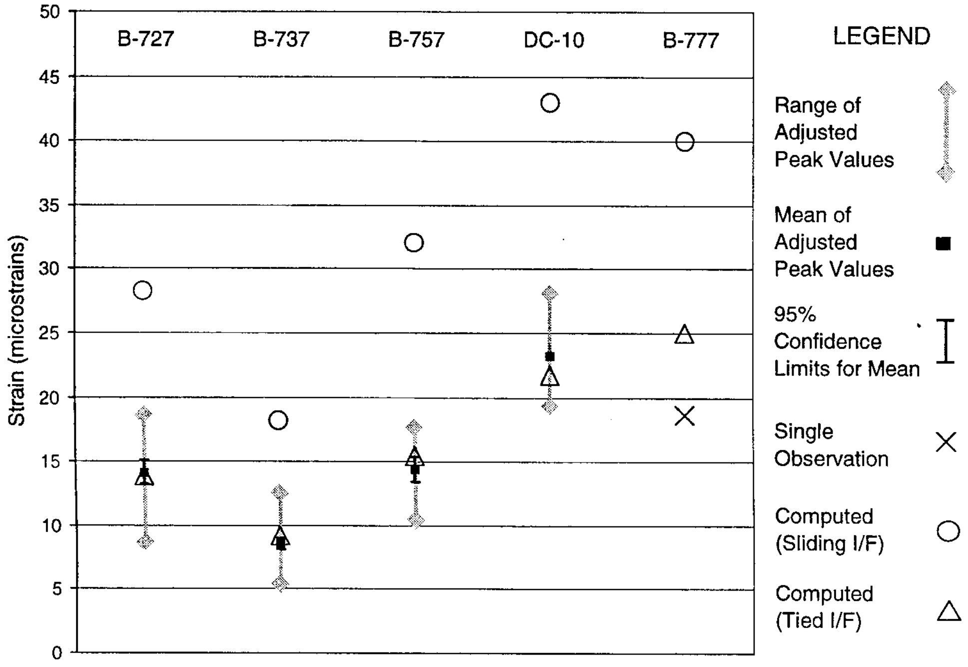

FIGURE 9. PEAK STRAIN RESPONSE AT STRAIN GAUGE H71 COMPARED TO 3D FINITE ELEMENT SOLUTION FOR VARIOUS AIRCRAFT TYPES

ANALYSIS OF VARIANCE.

Tables 2 through 4 and figures 7 through 9 are based on data collected in the months of January 1996, November to December 1996, and August 1997. Since strains measured in the slab interior are normally unaffected by seasonal variations in joint performance, separate analyses of the summer and winter gauge readings for interior gauges were not deemed necessary. However, in order to justify the assumption that the mean of peak strain at the slab interior is relatively constant throughout the year, an analysis was conducted of the B-737 data set only. The B-737 events were divided into three subsets, corresponding to the three time periods (January 1996, November to December 1996, and August 1997) and a separate mean and sample variance was calculated for each subset of events. For each pair of subsets, a two-tailed *t*-test (assuming equal population variance) was used to evaluate the "null" hypothesis, that the difference in the "true" mean for the two time periods being compared is zero. Rejection of the null hypothesis meant that the difference in the sample means was statistically significant at the 5 percent significance level (i.e., some seasonal influence on the interior peak strain could be inferred). A summary of the B-737 data analysis and *t*-tests is given in tables 6 through 8.

TABLE 6. STATISTICS FOR B-737 EVENTS BY SUBGROUP

Strain Gauge	Subgroup	Observations	Mean Strain (10^{-6})	Sample Variance (10^{-12})
H15	All Events	66	-11.634	3.919
	Subgroup 1 (January 1996)	40	-11.454	3.521
	Subgroup 2 (Nov.-Dec. 1996)	21	-12.213	3.997
	Subgroup 3 (August 1997)	5	-10.649	6.075
H70	All Events	66	-16.239	3.306
	Subgroup 1 (January 1996)	40	-15.915	2.475
	Subgroup 2 (Nov.-Dec. 1996)	21	-16.939	3.302
	Subgroup 3 (August 1997)	5	-15.993	9.295
H71	All Events	66	8.536	3.178
	Subgroup 1 (January 1996)	40	7.858	2.181
	Subgroup 2 (Nov.-Dec. 1996)	21	9.472	3.052
	Subgroup 3 (August 1997)	5	10.031	3.136

Table 7 indicates that the increase in mean peak strain observed between January 1996 and November to December 1996 for gauges H70 and H71 is statistically significant at the 5 percent level. In other words, it probably reflects an actual phenomenon, and not merely random fluctuation. The analysis provides no strong evidence to suggest that the mean peak strain at the interior of the slab is affected by the seasonal change from winter to summer, although the observed increase in mean peak strain at H71 from January 1996 to August 1997 (table 7) was found to be statistically significant at the 5 percent level.

Analysis of variance (ANOVA) for the three subgroups shows that variation between subgroups accounts for a relatively small proportion of the total variability (table 8). Statistical significance is indicated by $F > F_{critical}$. The *F*-test demonstrates that differences between subgroup means are not statistically significant (at the 5% level) for H15 and H70 data, but are statistically significant (at the 5% level) for H71.

TABLE 7. SUMMARY OF *t*-TEST FOR PAIRED SAMPLE MEANS

H-Bar Gauge No.	Result of t-test for $\alpha = 0.05$ μ_1 = Subgroup 1 μ_2 = Subgroup 2 $H_0 : \mu_1 - \mu_2 = 0$	 μ_1 = Subgroup 1 μ_2 = Subgroup 3 $H_0 : \mu_1 - \mu_2 = 0$	 μ_1 = Subgroup 2 μ_2 = Subgroup 3 $H_0 : \mu_1 - \mu_2 = 0$
H15	Do not reject H_0	Do not reject H_0	Do not reject H_0
H70	Do not reject H_0	Do not reject H_0	Do not reject H_0
H71	Reject H_0	Reject H_0	Do not Reject H_0

TABLE 8. ANALYSIS OF VARIANCE (ANOVA) FOR B-737 PEAK STRAIN

Strain Gauge	Source of Variation	ANOVA SS	Degs. of Freedom	Mean Squares	F (statistic)	P-value	F critical
H15	Between groups	13.190	2	6.595	1.720	0.18739	3.143
	Within groups	241.577	63	3.835	-	-	-
	Total	254.767	65	-	-	-	-
H70	Between groups	15.102	2	7.551	2.381	0.10069	3.143
	Within groups	199.757	63	3.171	-	-	-
	Total	214.859	65	-	-	-	-
H71	Between groups	47.954	2	23.977	9.522	0.00024	3.143
	Within groups	158.637	63	2.5180	-	-	-
	Total	206.591	65	-	-	-	-

EDGE LOADS.

Peak strains from seven H-Bar strain gauges were analyzed and compared to computed edge strains for various aircraft types. Three of the seven strain gauges (H13, H19, and H42) are located along the transverse joint connecting slabs D2 and D3 (Joint A in figure 1). The remaining four gauges (H16, H25, H26, and H45) are located along the transverse joint at the north side of slab D4 (Joint B in figure 1).

In contrast to the interior load case, the strains at gauges located near the slab edge depend on the joint performance. Other conditions being equal, a better performing joint will result in lower peak edge strains than a poorly performing joint, due to additional load transfer from the loaded slab to the unloaded slab. In-service load transfer at the slab edge is directly affected by several variables, including:

1. The type of joint construction (doweled, hinged, keyed, etc.).
2. The amount of deterioration at the joint.
3. The arrangement and orientation of wheels in the loading gear.

4. The degree of aggregate interlock achieved at the joint (which in turn may depend on temperature and other environmental variables).

The DIA test pavement includes several types of joint construction. Figure 10 shows the various types of joint construction used within the 16-slab test area. Transverse joints in the test area interior, including joint A in figure 1, are "dummy" joints, i.e., joints constructed without dowels, keys, or other mechanical load transfer devices. Load transfer at the interior transverse joints is achieved by aggregate interlock between adjoining slabs and, to a lesser extent, by shear transfer in the stabilized base layer. Since cooler temperatures cause the concrete slabs to contract and separate, thereby reducing aggregate interlock, it is expected that reduced load transfer during the winter months will lead to higher peak strains in the winter months than in the summer months.

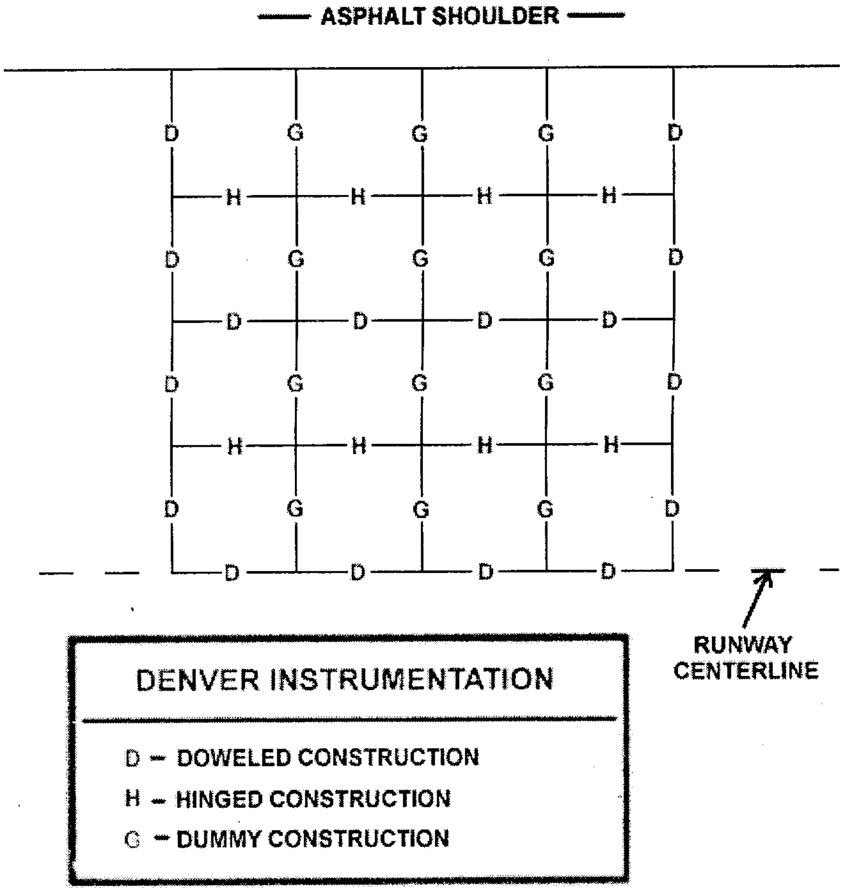

FIGURE 10. JOINT CONSTRUCTION IN DIA INSTRUMENTED RUNWAY

Transverse joints located on the north and south boundaries of the instrumented area, including joint B in figure 1, are of doweled construction. It is expected that the doweled joints are less sensitive than the dummy joints to changes in temperature. Nevertheless, because aggregate interlock as well as dowel action contributes to the load transfer at the doweled joint, it is also true that the doweled joints may be affected by seasonal changes to an unknown degree.

In the analysis that follows, it was initially assumed that the average peak strain at the slab edge is indirectly a function of the time of year in which measurements are taken, i.e., higher average strains are expected to occur during the cooler winter months because of reduced joint efficiency. To test the validity of this assumption, mean peak strains were evaluated for the individual months in which they were collected, as well as for the entire 20-month data collection period. Data sets were constructed from stored data using the online query method described in an earlier section. As in the earlier section, events from the database were included in the data set for a particular H-bar strain gauge H*xx* only if:

- The database table called *hbxx* contained a peak value for the event.
- The aircraft type for the data set matched the text in the *aircrafttype* field for the event. For example, the B-737 data sets included events containing B-737, B-737-100, B-737-200, etc., in the *aircrafttype* field.
- The event occurred in a specific month/year time frame.
- Events that met the above conditions were excluded from the data set if:
- It was determined from subsequent position sensor analysis that the aircraft wheel did not cover the strain gauge.
- The *aircraftweight* field for the event was null, indicating that the gross weight of the aircraft was not known.

Once the event data sets were established for each aircraft type, the peak strain readings for each data set were adjusted to a uniform weight basis using the adjustment factor in equation 1. As in the interior load analysis, the value of w_{FEA} for each aircraft type is the gross aircraft weight used in the finite element analysis. The 95% confidence limits for the mean were calculated using equation 2. However, 95% confidence limits were not calculated for fewer than five events in the data set.

Tables 9 through 12 summarize the B-727 peak strain statistics for the seven H-bar gauges on a comparative month-by-month basis. Unfortunately, data was not available for all months. Complete data (including gross aircraft weights) was available for events only in the following months: January 1996, February 1996, November 1996, December 1996, and August 1997. Furthermore, the available events were not evenly distributed among those five months, with the total sample heavily weighted toward January 1996.

TABLE 9. DISTRIBUTION OF PEAK STRAIN EVENTS BY MONTH (B-727)

Gauge Number	Number of Events (B-727 Events)					
	Jan 96	Feb 96	Nov 96	Dec 96	Aug 97	All Events
H13	40	29	0	0	1	70
H16	37	0	0	18	5	60
H19	40	29	20	8	1	98
H25	37	0	0	18	5	60
H26	48	0	0	15	3	66
H42	40	29	20	8	1	98
H45	48	0	0	15	3	66

TABLE 10. PEAK STRAIN SAMPLE MEAN BY MONTH (B-727 EVENTS)

Gauge Number	Mean Adjusted Peak Strain (10^{-6})					
	Jan 96	Feb 96	Nov 96	Dec 96	Aug 97	All Events
H13	-22.021	-21.630	N/A	N/A	-20.250	-21.834
H16	-32.310	N/A	N/A	-28.454	-26.706	-30.686
H19	28.032	29.949	31.034	30.895	31.735	29.483
H25	21.113	N/A	N/A	14.828	27.381	19.750
H26	19.818	N/A	N/A	19.786	23.062	19.958
H42	-22.234	-22.477	-21.370	-23.349	-16.794	-22.165
H45	-31.832	N/A	N/A.	-30.888	-29.164	-31.496

TABLE 11. PEAK STRAIN SAMPLE VARIANCE BY MONTH (B-727 EVENTS)

Gauge Number	Sample Variance (10^{-12})					
	Jan 96	Feb 96	Nov 96	Dec 96	Aug 97	All Events
H13	7.493	7.202	(no data)	(no data)	*	7.232
H16	25.644	(no data)	(no data)	12.952	21.847	25.378
H19	17.292	9.305	14.091	21.988	*	15.632
H25	26.802	(no data)	(no data)	11.852	20.283	34.636
H26	26.766	(no data)	(no data)	55.846	*	33.037
H42	4.728	5.100	11.885	8.902	*	6.918
H45	24.146	(no data)	(no data)	52.932	*	29.680

* insufficient number of observations

TABLE 12. CONFIDENCE LIMITS (95%) FOR MEAN OF PEAK STRAIN
BY MONTH (B-727 EVENTS)

Gauge Number	95% Confidence Limits for Mean of Peak Strain (10^{-6})							
	Jan 96		Feb 96		Nov 96		Dec 96	
	Limit	(±)	Limit	(±)	Limit	(±)	Limit	(±)
H13	-22.02	0.88	-21.63	1.02	(no data)		(no data)	
H16	-32.31	1.69	(no data)		(no data)		-28.45	1.79
H19	28.03	1.33	29.95	1.16	31.04	1.76	30.9	3.93
H25	21.12	1.73	(no data)		(no data)		14.83	1.71
H26	19.82	1.5	(no data)		(no data)		19.79	4.14
H42	-22.23	0.7	-22.48	0.86	-21.37	1.61	-23.34	2.5
H45	-31.83	1.43	(no data)		(no data)		-30.89	4.03
	Aug 97		(not used)		(not used)		All Events	
	Limit	(±)					Limit	(±)
H13	*						-21.83	0.65
H16	-26.7	5.81					-30.68	1.31
H19	*						29.49	0.8
H25	27.38	5.59					19.75	1.52
H26	*						19.96	1.41
H42	*						-22.16	0.53
H45	*						-31.5	1.34

* insufficient number of observations

The above analysis does not provide statistical evidence supporting the hypothesized trend toward higher peak strains in the winter months. In fact, for gauge H25 a sharply higher mean peak strain was observed for August 1997 than for the previous (winter) months, but it is believed that this counterintuitive result is a statistical anomaly due to the small number of observations in August, rather than a real trend. Excluding the month of August 1997, where no more than five usable events were identified for any aircraft type, it was found that the differences in the calculated mean peak strain taken from month to month, and for individual months as compared to the total data set, were not statistically significant at the 5 percent significance level. (Again, the one exception was H25, where table 12 shows a statistically significant reduction in mean peak strain from January 1996 to December 1996.) Based on the results of the preceding analysis, the use of mean strain values based on the total data set for comparison to finite element strains was justified.

Tables 13 through 19 summarize statistics for peak strain data collected at each of the seven H-bar strain gauges (H13, H19, and H42 at joint A (dummy) and H16, H25, H26, and H45 at joint B (doweled)) for all events. Tables 20 and 21 list finite element strains computed in the slab at the various H-bar gauge locations using the 3D finite element edge strain model. Table 20 lists strains computed on the assumption of a zero-bond interface, with layer separation allowed to occur between the base and the unloaded PCC slab. Table 21 strains were computed on the basis of a fully bonded interface.

TABLE 13. SUMMARY STATISTICS FOR PEAK STRAIN AT H13

Aircraft Type	Count (n)	Aircraft Wt., lbs.		Adjusted Peak Strain (10^{-6})			95% Confidence Limits for Mean (±)
		Avg. w_g	w_{FEA}	Mean	Range	Variance (10^{-12})	
B-727	70	162,484	172,000	-21.83	12.39	7.23	0.65
B-737	64	108,963	100,000	-13.94	11.92	5.63	0.6
B-757	9	187,916	250,000	-29.57	17.43	29.83	4.2
DC-10	3	362,003	458,000	-38.38	-	-	-
B-777	0	-	634,500	-	-	-	-

TABLE 14. SUMMARY STATISTICS FOR PEAK STRAIN AT H19

Aircraft Type	Count (n)	Aircraft Wt., lbs.		Adjusted Peak Strain (10^{-6})			95% Confidence Limits for Mean (±)
		Avg. w_g	w_{FEA}	Mean	Range	Variance (10^{-12})	
B-727	98	161,728	172,000	29.48	20.58	15.63	0.8
B-737	90	108,134	100,000	18.85	15.08	7.88	0.59
B-757	10	187,951	250,000	33.08	14.22	22.66	3.41
DC-10	3	362,003	458,000	42.45	-	-	-
B-777	0	-	634,500	-	-	-	-

TABLE 15. SUMMARY STATISTICS FOR PEAK STRAIN AT H42

Aircraft Type	Count (n)	Aircraft Wt., lbs.		Adjusted Peak Strain (10^{-6})			95% Confidence Limits for Mean (±)
		Avg. w_g	w_{FEA}	Mean	Range	Variance (10^{-12})	
B-727	98	161,728	172,000	-22.16	14.52	6.92	0.53
B-737	90	108,134	100,000	-13.14	14.93	5.11	0.48
B-757	10	187,951	250,000	-27.05	8.79	11.83	2.46
DC-10	3	362,003	458,000	-38.42	-	-	-
B-777	0	-	634,500	-	-	-	-

TABLE 16. SUMMARY STATISTICS FOR PEAK STRAIN AT H16

Aircraft Type	Count (n)	Aircraft Wt., lbs.		Adjusted Peak Strain (10^{-6})			95% Confidence Limits for Mean (±)
		Avg. w_g	w_{FEA}	Mean	Range	Variance (10^{-12})	
B-727	60	159,523	172,000	-30.69	25.35	25.38	1.31
B-737	73	109,013	100,000	-19.65	18.12	17.12	0.97
B-757	12	191,457	250,000	-31.49	24.02	72.71	5.42
DC-10	0	-	458,000	-	-	-	-
B-777	0	-	634,500	-	-	-	-

TABLE 17. SUMMARY STATISTICS FOR PEAK STRAIN AT H25

Aircraft Type	Count (n)	Aircraft Wt., lbs.		Adjusted Peak Strain (10^{-6})			95% Confidence Limits for Mean (±)
		Avg. w_g	w_{FEA}	Mean	Range	Variance (10^{-12})	
B-727	60	159,523	172,000	19.75	24.39	34.64	1.52
B-737	73	109,013	100,000	13.68	13.77	14.61	0.9
B-757	12	191,457	250,000	22.38	21.55	65.57	5.15
DC-10	0	-	458,000	-	-	-	-
B-777	0	-	634,500	-	-	-	-

TABLE 18. SUMMARY STATISTICS FOR PEAK STRAIN AT H26

Aircraft Type	Count (n)	Aircraft Wt., lbs.		Adjusted Peak Strain (10^{-6})			95% Confidence Limits for Mean (±)
		Avg. w_g	w_{FEA}	Mean	Range	Variance (10^{-12})	
B-727	66	160,021	172,000	19.96	23.37	33.04	1.41
B-737	77	110,042	100,000	14.70	22.24	22.14	1.07
B-757	5	190,556	250,000	20.23	20.46	57.58	9.42
DC-10	0	-	458,000	-	-	-	-
B-777	0	-	634,500	-	-	-	-

TABLE 19. SUMMARY STATISTICS FOR PEAK STRAIN AT H45

Aircraft Type	Count (n)	Aircraft Wt., lbs.		Adjusted Peak Strain (10^{-6})			95% Confidence Limits for Mean (±)
		Avg. w_g	w_{FEA}	Mean	Range	Variance (10^{-12})	
B-727	66	160,021	172,000	-31.50	24.95	29.68	1.34
B-737	77	110,042	100,000	-21.32	21.93	19.19	0.99
B-757	5	190,556	250,000	-31.16	22.16	66.90	10.16
DC-10	0	-	458,000	-	-	-	-
B-777	0	-	634,500	-	-	-	-

TABLE 20. COMPUTED STRAINS FOR EDGE STRAIN COMPARISON
(ZERO BOND INTERFACE MODEL)

Aircraft Type	3D Finite Element Computed Strain (10^{-6})						
	Doweled Joint				Dummy Joint		
	H16	H25	H26	H45	H13	H19	H42
B-727	-32.37	38.32	36.91	-31.15	-24.82	37.90	-22.61
B-737	-22.38	26.20	25.81	-21.63	-16.39	26.78	-16.01
B-757	-36.61	42.77	42.28	-35.51	-27.11	41.11	-24.57
DC-10	-	-	56.59	-47.67	-	54.81	-32.87
B-777	-	-	-	-	-	-	-

TABLE 21. COMPUTED STRAINS FOR EDGE STRAIN COMPARISON (FULL BOND INTERFACE MODEL)

Aircraft Type	3D Finite Element Computed Strain (10^{-6})						
	Doweled Joint				Dummy Joint		
	H16	H25	H26	H45	H13	H19	H42
B-727	-23.55	17.98	17.74	-22.67	-18.11	17.54	-16.75
B-737	-15.76	12.46	12.34	-15.22	-12.02	12.07	-11.10
B-757	-27.12	19.19	19.10	-26.31	-21.09	18.92	-19.57
DC-10	-48.78	25.6	25.57	-47.39	-38.79	26.15	-27.32
B-777	-	-	-	-	-	-	-

The computed strains reported in tables 20 and 21 are the maximum strains under the tire at the vertical location corresponding to the installed depth of the H-bar strain gauge. In all cases, the computed strain is in the direction parallel to the transverse joint. For all computations, the base layer was assumed continuous (monolithic) under joints. Other material properties were as listed in table 1. A PCC slab thickness equal to the actual slab depth measured at the H-bar strain gauge location was used for the computations. Slab thickness and gauge depths for the seven strain gauges in tables 20 and 21 are listed in table 22.

TABLE 22. PCC SLAB THICKNESSES AND GAUGE DEPTHS

H-Bar Gauge No.	PCC Thickness, in.	Top or Bottom of Slab	Depth of Gauge, in.
H13	18.20	Top	3.83
H16	17.15	Top	2.15
H19	18.27	Bottom	17.27
H25	17.15	Bottom	16.15
H26	17.49	Bottom	16.49
H42	18.27	Top	4.33
H45	17.49	Top	2.30

For gauges located at doweled joints, the equivalent vertical spring constant of the joint (k_{jnt}) was calculated from known dowel bar data using the method described in Ioannides and Korovesis [5]. In this method, the elastic stiffness provided by a dowel bar is assumed to be

$$k_{jnt} = \frac{1}{s\left(\frac{2}{K_1} + \frac{1}{K_2}\right)} \tag{3}$$

where s is the dowel bar spacing, K_1 is the stiffness contribution from dowel-concrete interaction, given by

$$K_1 = \frac{P_t}{\Delta_o} = \frac{4\beta^3}{2 + \beta\omega} E_d I_d \tag{4}$$

and K_2 is the stiffness contribution due to bending action of the dowel bar

$$K_2 = \frac{12E_d I_d}{\omega^3(1+\phi)} \tag{5}$$

In equations 4 and 5 above, the following symbols are used: P_t is the load transferred by one dowel bar; Δ_o is the deflection of the bar at the face of the slab due to bearing of the bar on the concrete; E_d is the Young's modulus of the dowel bar material (29,000,000 psi for mild steel); I_d is the moment of inertia of the dowel bar section; ω is the joint opening; β is a dimensionless "relative stiffness" defined by

$$\beta = \sqrt[4]{\frac{K_d d}{4E_d I_d}} \tag{6}$$

where d is the dowel bar diameter and K_d is a modulus of reaction of the dowel bar on the concrete; and ϕ is a shear factor defined by

$$\phi = \frac{12E_d I_d}{0.9G_d A_d \omega^2} \tag{7}$$

where G_d is the shear modulus of the dowel bar material, A_d is the cross-sectional area of the dowel bar, and the 0.9 term is a shear correction factor.

Making the substitutions in equation 3 gives

$$k_{jnt} = \frac{1}{s\left(\frac{\omega}{0.9G_d A_d} + \frac{\omega^3}{12E_d I_d} \frac{2+\beta\omega}{2\beta^3 E_d I_d}\right)} \tag{8}$$

It should be noted that equation 3 is corrected from the similar equation that appears in reference 5 to account for the bearing reaction on both ends of the dowel bar, Brill and Guo [6]. Equation 8 was implemented in the computer program that automatically generates 3D meshes and input files for 3D finite element analysis. For doweled joints in the DIA runway, the following input values were used: $d = 1.5$ in (3.81 cm); $s = 18$ in (45.1 cm); $\omega = 0.125$ in (3.2 mm). Based on results given by Hammons and Freeman [7] for dowel bars placed in fresh concrete, the program assumes that the modulus of dowel bar reaction is 8,290,000 lb/in^2/in (2,250 GPa/m). Using the above input values, the value of joint stiffness computed for doweled joints at DIA was 197,731 lbs/in^2 (1,363 MPa). For nondoweled (dummy) joints, the default value k_{jnt} = 100,000 lb/in^2 (690 MPa) was used.

Data from tables 13 through 21 was used to plot the peak strain comparisons in figures 11 through 17.

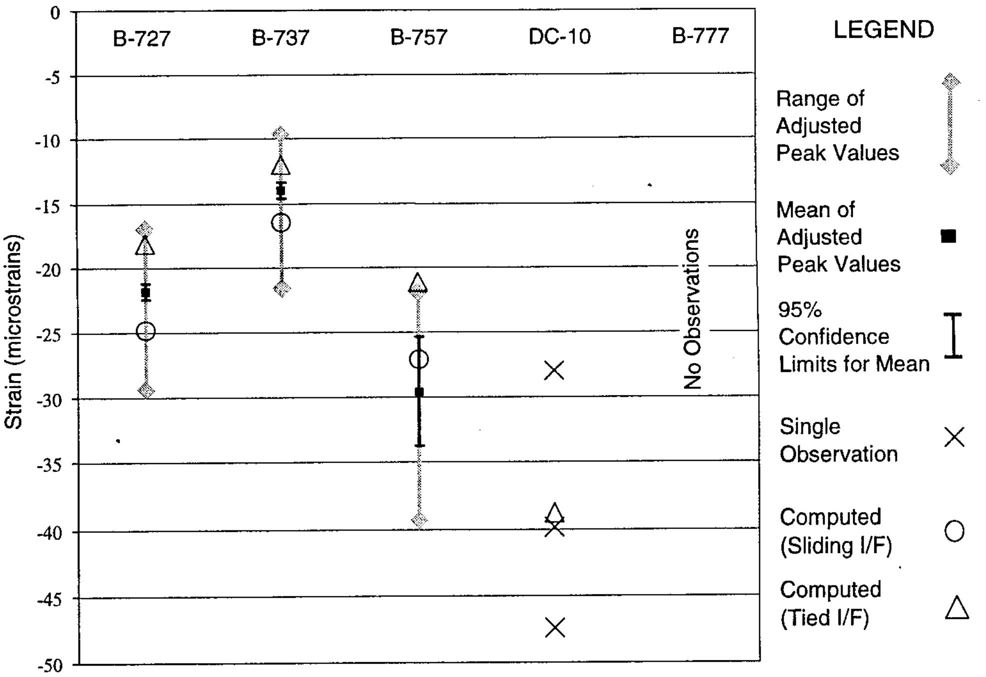

FIGURE 11. PEAK STRAIN RESPONSE AT STRAIN GAUGE H13 (DUMMY JOINT) COMPARED TO 3D FINITE ELEMENT SOLUTION FOR VARIOUS AIRCRAFT TYPES

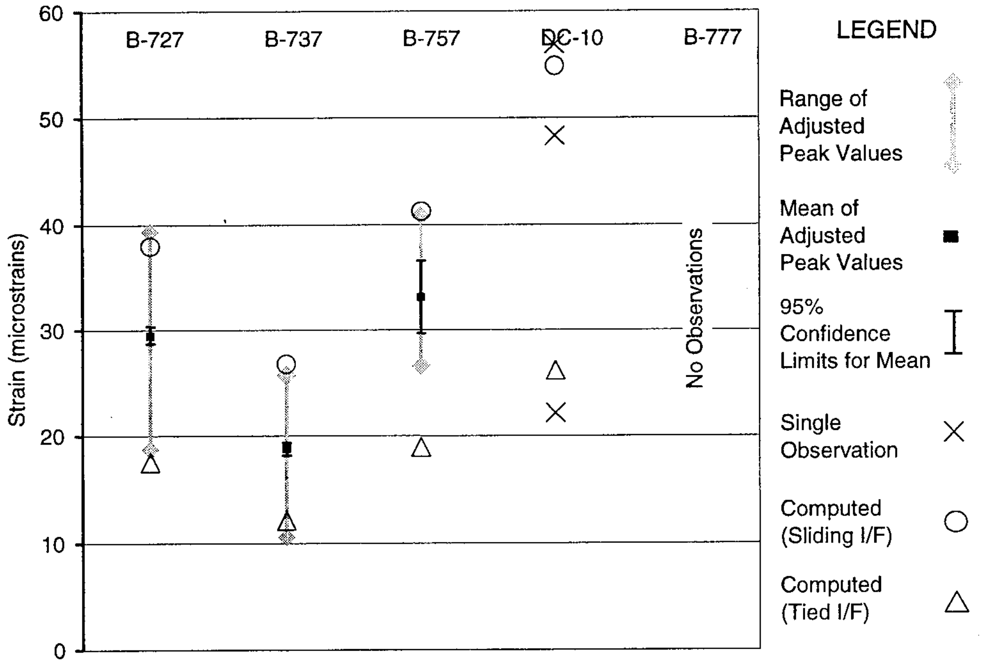

FIGURE 12. PEAK STRAIN RESPONSE AT STRAIN GAUGE H19 (DUMMY JOINT) COMPARED TO 3D FINITE ELEMENT SOLUTION FOR VARIOUS AIRCRAFT TYPES

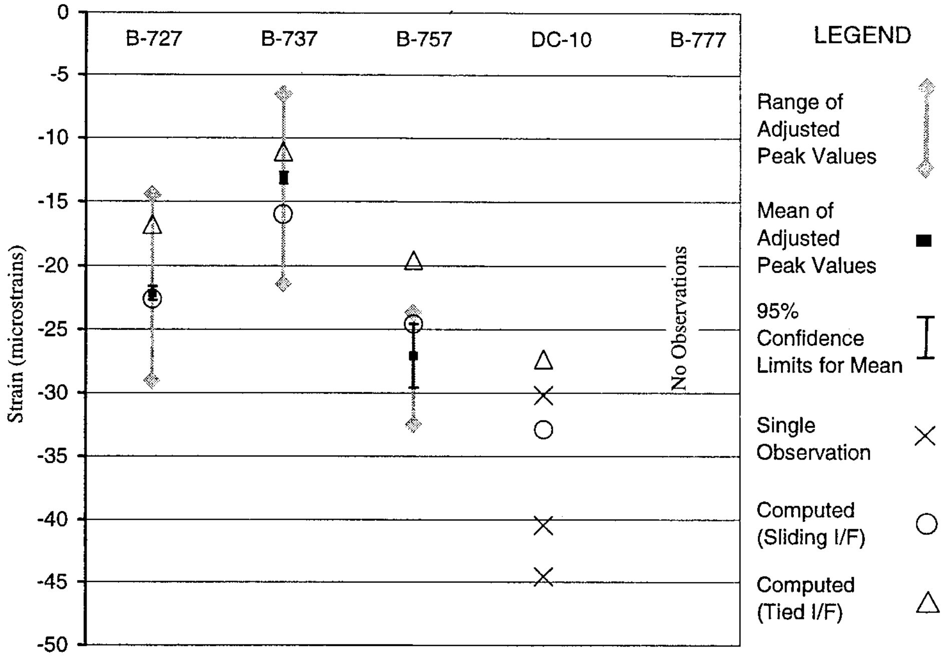

FIGURE 13. PEAK STRAIN RESPONSE AT STRAIN GAUGE H42 (DUMMY JOINT) COMPARED TO 3D FINITE ELEMENT SOLUTION FOR VARIOUS AIRCRAFT TYPES

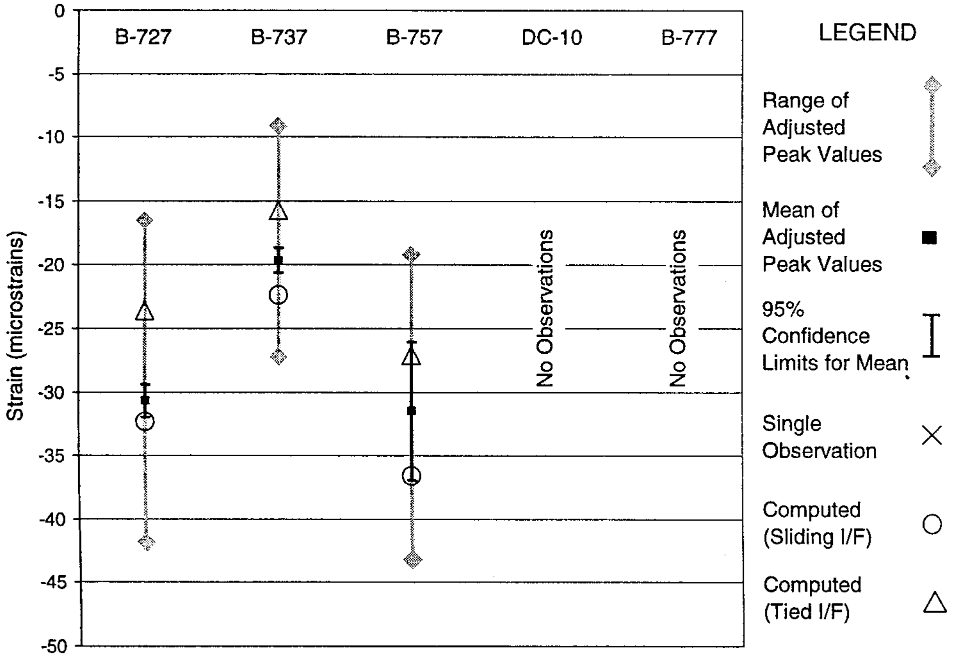

FIGURE 14. PEAK STRAIN RESPONSE AT STRAIN GAUGE H16 (DOWELED JOINT) COMPARED TO 3D FINITE ELEMENT SOLUTION FOR VARIOUS AIRCRAFT TYPES

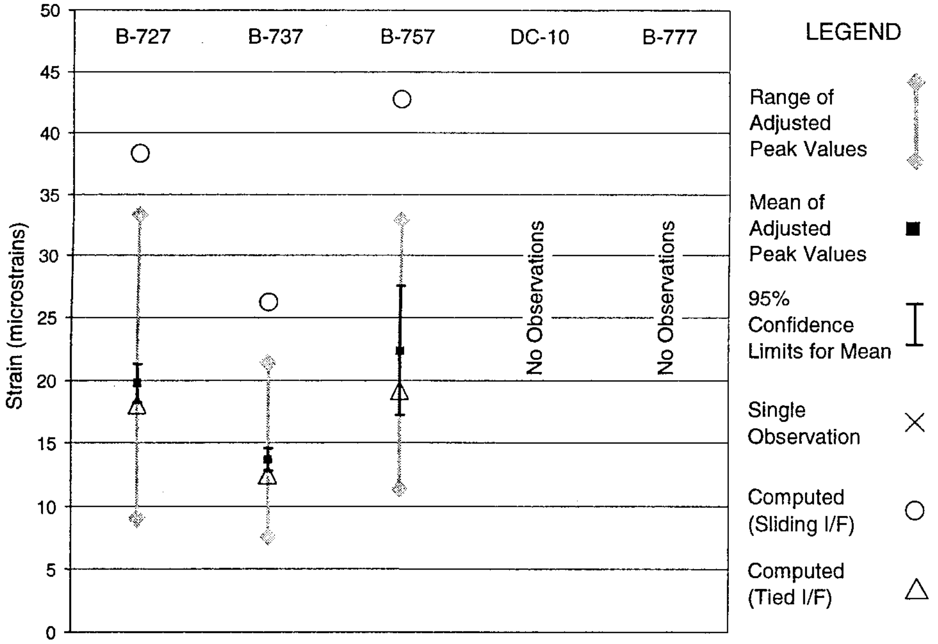

FIGURE 15. PEAK STRAIN RESPONSE AT STRAIN GAUGE H25 (DOWELED JOINT) COMPARED TO 3D FINITE ELEMENT SOLUTION FOR VARIOUS AIRCRAFT TYPES

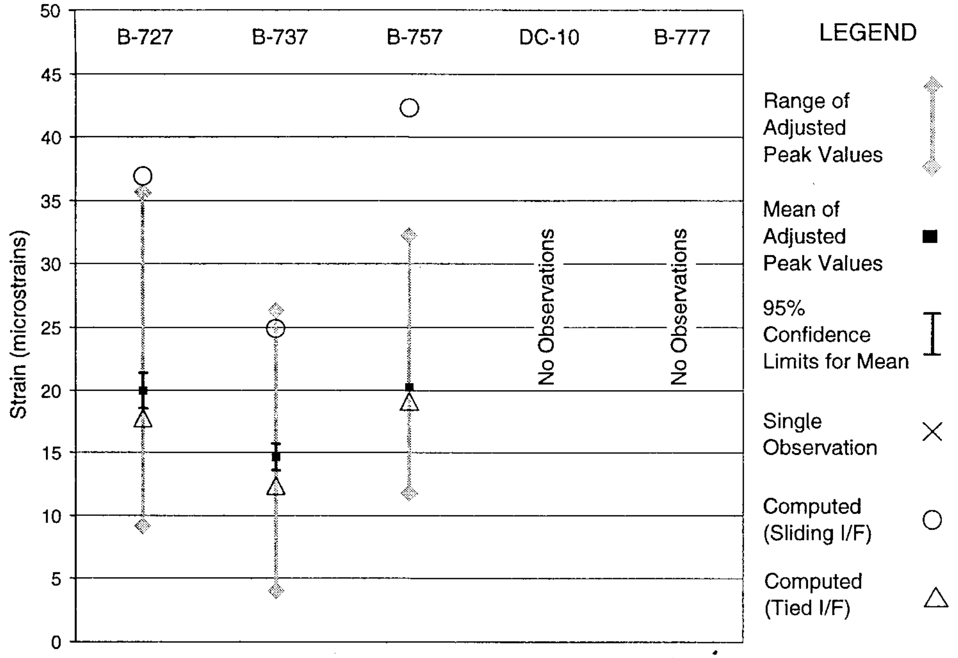

FIGURE 16. PEAK STRAIN RESPONSE AT STRAIN GAUGE H26 (DOWELED JOINT) COMPARED TO 3D FINITE ELEMENT SOLUTION FOR VARIOUS AIRCRAFT TYPES

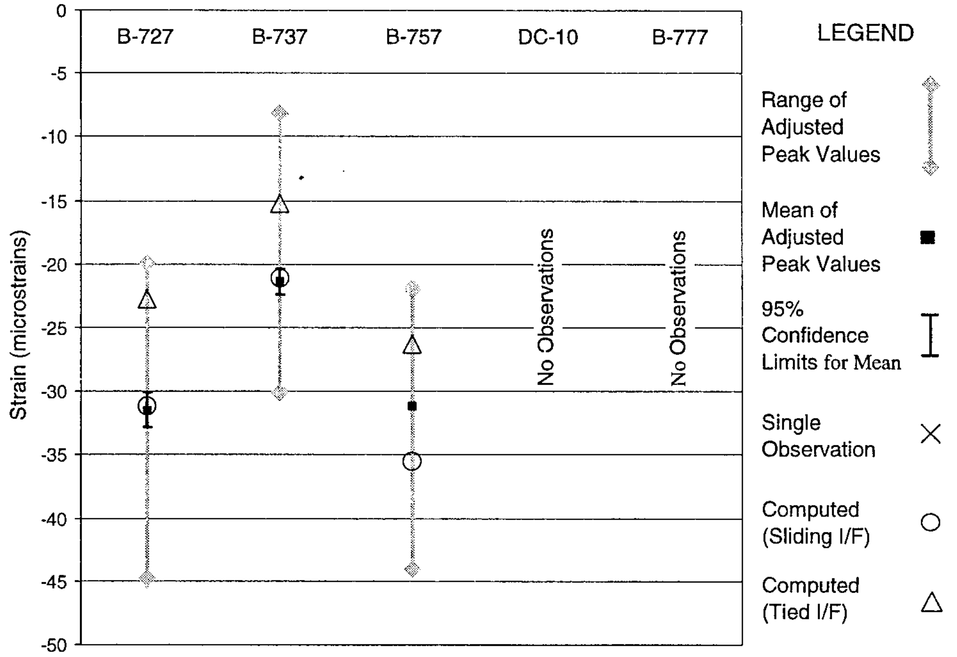

FIGURE 17. PEAK STRAIN RESPONSE AT STRAIN GAUGE H45 (DOWELED JOINT) COMPARED TO 3D FINITE ELEMENT SOLUTION FOR VARIOUS AIRCRAFT TYPES

The following observations are made from figures 11 through 17:

1. There is a very wide range of peak strain values for all gauges and aircraft types for which data was obtained. Therefore, taking any particular H-bar strain gauge reading as representative of the typical strain response at that location could be highly misleading.

2. The mean peak strain responses for gauges near the top of the concrete slab (H13, H16, H42, and H45) generally were found to be close to the computed values of edge strain. In many cases the finite element computed strain fell within the 95 percent confidence limits for the mean of peak strain calculated from gauge data. In these cases, the computed strain was based on the fully unbonded interface. However, the interface model (fully bonded versus unbonded) had a relatively small effect on computed top-of-slab strain compared to gauges near the bottom.

3. The mean peak strain responses for gauges located near the bottom of the concrete slab (H19, H25, and H26) generally fell between the computed values of edge strain for the tied interface and sliding interface models. This result may be interpreted as evidence of partial bonding between the concrete slab and CTB layers. For gauges located along transverse joint B (doweled joint), it was found that the mean peak strain from gauge data was much closer to the full bond case than to the sliding case.

PEAK DEFLECTION COMPARISONS

Eighteen LVDTs measure dynamic vertical displacements of the concrete slab at DIA runway 34R-16L. Of the 18 LVDTs in the slab, 9 are single-depth deflectometer (SDD) gauges and 9 are component gauges within multiple-depth deflectometers (MDDs). Each of the nine MDD sensors at DIA consists of a series of four LVDTs, of which one gauge (gauge 1) is located in the slab and three gauges (gauges 2, 3, and 4) are at levels below the slab. The locations of all LVDT gauges, both SDD and MDD, are shown in figure 2. All of the MDD gauges are anchored at approximately 10 ft (3.05 m) below grade. The approximate anchor depth for SDD gauges is either 10 ft (3.05 m) or 20 ft (6.1 m), as shown in figure 2. For aircraft loads, a significant portion of the vertical strain contributing to the total deflection occurs at depths below the anchor. Thus, the LVDT reading gives the vertical displacement relative to the anchor displacement, which is always less than the absolute vertical displacement. The difference between the LVDT reading and the absolute displacement must be taken into account when analyzing the displacement data.

For each aircraft event (designated by a unique event number, *event#*), peak displacement responses from up to 10 LVDT gauges are stored in the database. As with the peak strain data, the peak displacement responses are stored in Oracle tables, with one table for each LVDT gauge. For example, all peak displacement responses of MDD6, LVDT gauge 1, are stored in a table named *mdd6g1*. Figure 18 shows a typical LVDT record for a B-777 event. Similar to the strain record for the same event (figure 5), the displacement record exhibits three local peaks corresponding to the three main gear axles of the B-777 aircraft. Of the three peaks, only the largest (global) peak value is stored in the database.

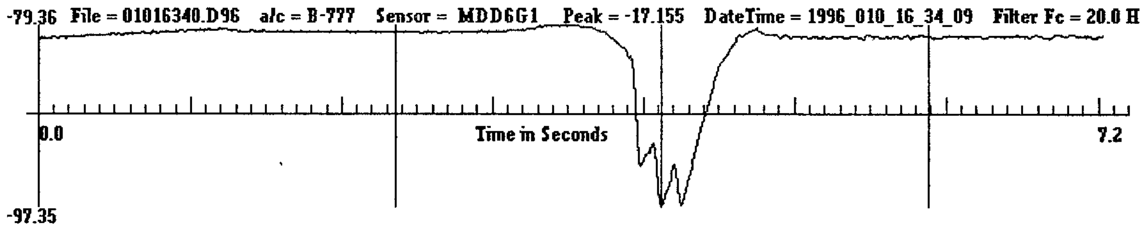

FIGURE 18. DYNAMIC DISPLACEMENT OF MDD6G1, GAUGE 1
(B-777 DEPARTURE)

The procedure for querying the online database is described in detail in the section on "Peak Strain Comparisons." Peak deflection events for various aircraft types were selected from the database using SQL commands as shown previously, except that the names of H-bar sensor tables *hb1*, *hb2*, etc., were replaced with the appropriate LVDT sensor table names. As in the previous case involving peak strain, the position sensor responses were used to identify particular events for which the aircraft tire covered the LVDT sensor. Events for which the tire did not cover the sensor, as determined from position sensor responses, were eliminated from the data sets.

Mean values of peak deflection calculated from the selected DIA data were compared to computed static deflection results from the 3D finite element model. Material properties for the finite element analysis are listed in table 1. All finite element calculations assumed a fixed base at the 120-inch (10-foot, 3.05-m) depth; hence, the finite element deflection results are comparable to LVDT readings from those gauges with a 10-foot (3.05-m) anchor.

INTERIOR LOADS.

Interior load peak deflection comparisons are based on the responses of DIA sensor MDD8 (gauge 1). As shown in figure 2, this MDD is anchored at a depth of 10 feet (3.05 m). Hence, the peak deflection readings from MDD8 are comparable to the displacement in pavement structure from the surface to a 10-foot (3.05-m) depth evaluated by the 3D finite element program (interior load condition).

Table 23 summarizes the statistical analysis of MDD8 peak responses. Responses are broken down by aircraft type. No attempt was made to break down responses according to month or season. For each of the four aircraft types included in the analysis (B-727, B-737, B-757, and DC-10) the event count (*n*) is the total number of events returned by the following online query of the database (less the number of duplicate events and events for which the tire did not cover the MDD sensor location):

TABLE 23. SUMMARY STATISTICS FOR PEAK DEFLECTION AT MDD8G1

Aircraft Type	Count (n)	Aircraft Weight (lbs.)		Adjusted Peak Deflection (mils)			95% Confidence Limits for Mean (±)
		avg. w_g	w_{FEA}	Mean	Range	Variance mils^2	
B-727	72	160,657	172,000	-7.067	2.714	0.2957	0.128
B-737	112	108,274	100,000	-4.455	3.297	0.2663	0.096
B-757	6	186,408	250,000	-9.108	1.089	0.1480	0.403
DC-10	2	364,728	458,000	-15.10	-	-	-

Query 1:

```
select aircraft.event#, datetime, aircraftweight, mdd8g1.peak1
from aircraft, mdd8g1, p5, p26
where aircrafttype = [substitute aircraft type here]
and aircraft.event# = mdd8g1.event#
and aircraft.event# = p5.event# and aircraft.event# = p26.event#
and aircraftweight > 0;
```

Query 2:

```
select aircraft.event#, datetime, aircraftweight, mdd8g1.peak1
from aircraft, mdd8g1, p6, p25
where aircrafttype = [substitute aircraft type here]
and aircraft.event# = mdd8g1.event#
and aircraft.event# = p6.event# and aircraft.event# = p25.event#
and aircraftweight > 0;
```

An adjusted peak deflection for each event was computed using the adjustment factor defined by the formula in equation 1. The adjusted mean peak and 95% confidence limits for the mean were computed for each of the first three aircraft categories. Statistics were not computed for the DC-10 group, due to the small number of DC-10 events returned.

Figure 19 and table 24 compare the group means from table 23 to the corresponding 3D finite element solutions. Two finite element cases are considered: (a) zero bond at the slab-base interface (sliding interface) and (b) full bond at the slab-base interface (tied).

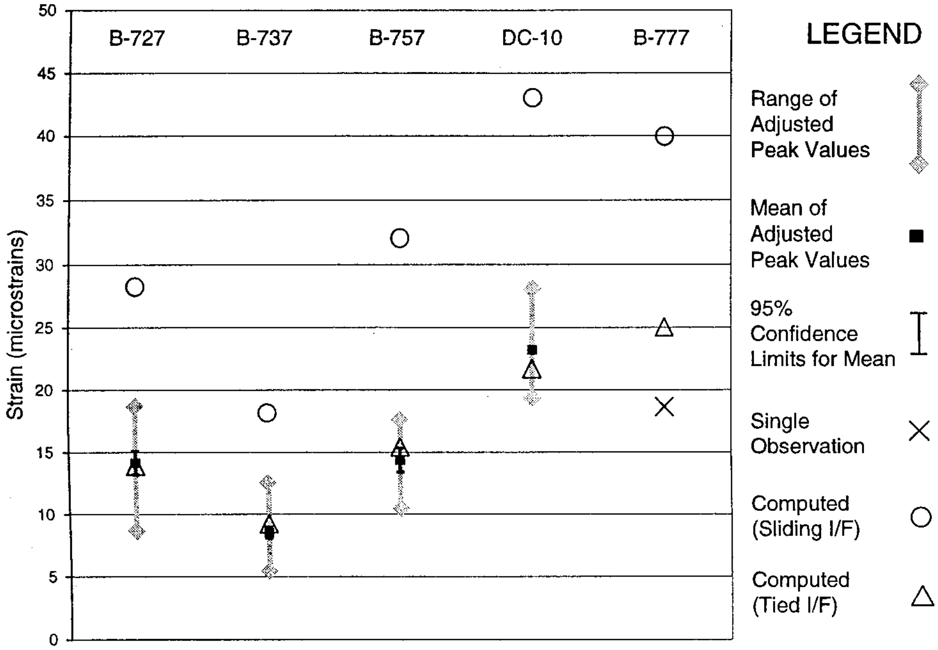

FIGURE 19. PEAK DEFLECTION OF SLAB AT MDD8 (GAUGE 1) COMPARED TO 3D FINITE ELEMENT SOLUTION FOR VARIOUS AIRCRAFT TYPES

TABLE 24. PEAK DEFLECTION COMPARISON (INTERIOR LOAD CASE)

Aircraft Type	Mean Adjusted Peak Deflection at MDD8G1, in $\cdot 10^3$	3D Finite Element Deflection, mils	
		Sliding Interface	Tied Interface
B-727	-7.067	-12.57	-9.05
B-737	-4.455	-7.43	-5.38
B-757	-9.108	-16.06	-12.01
DC-10	-15.10	-24.59	-19.33

Figure 19 demonstrates that the finite element computed deflections are significantly closer to the observed mean deflections if the model assumes a tied interface rather than a sliding interface. The finite element model was found to over predict deflections for both cases, but the amount of the over prediction was much less for the tied interface case.

EDGE LOADS.

Peak deflection comparisons for edge loads are based on the responses of DIA sensors MDD6 (gauge 1) and SDD17. Sensors MDD6 and SDD17 are located on the north and south sides, respectively, of the undoweled transverse joint at the junction of slabs D2 and D3 (figure 2). Both gauges are anchored at a depth of 10 feet (3.05 m). Hence, the peak deflection readings from MDD6 and SDD17 are comparable to the 3D finite element interior load solution when a 10-foot (120-inch, 3.05-m) depth of subgrade is assumed.

Tables 25 and 26 summarize the statistical analyses of MDD6 and SDD17 peak responses. Responses are broken down by aircraft type. No attempt was made to break down responses according to month or season. For each of the four aircraft types included in the analysis (B-727, B-737, B-757, and DC-10) the event count (*n*) is the total number of events returned by an online query of the database (less the number of duplicate events and events for which the tire did not cover the LVDT sensor location). The following examples of query operations return B-727 events for MDD6 (gauge 1).

TABLE 25. SUMMARY STATISTICS FOR PEAK DEFLECTION AT MDD6G1

Aircraft Type	Count (*n*)	Aircraft Weight (lbs.) avg. w_g	Aircraft Weight (lbs.) w_{FEA}	Adjusted Peak Deflection (mils) Mean	Adjusted Peak Deflection (mils) Range	Adjusted Peak Deflection (mils) Variance mils^2	95% Confidence Limits for Mean (±)
B-727	40	160,028	172,000	-13.44	10.066	6.0097	0.785
B-737	64	107,500	100,000	-9.661	10.569	5.2799	0.572
B-757	11	187,904	250,000	-19.36	11.666	14.7618	2.58
DC-10	5	354,569	458,000	-28.32	10.691	-	-

TABLE 26. SUMMARY STATISTICS FOR PEAK DEFLECTION AT SDD17

Aircraft Type	Count (*n*)	Aircraft Weight (lbs.) avg. w_g	Aircraft Weight (lbs.) w_{FEA}	Adjusted Peak Deflection (mils) Mean	Adjusted Peak Deflection (mils) Range	Adjusted Peak Deflection (mils) Variance mils^2	95% Confidence Limits for Mean (±)
B-727	40	160,028	172,000	-13.48	8.622	4.5782	0.685
B-737	64	107,500	100,000	-9.241	10.713	4.0046	0.5
B-757	11	187,904	250,000	-18.47	10.448	11.3699	2.265
DC-10	5	354,569	458,000	-26.59	8.909	-	-

Query 1:

```
select aircraft.event#, datetime, aircraftweight, mdd6g1.peak1
from aircraft, mdd6g1, p8, p29
where (aircrafttype = 'B-727' or aircrafttype = 'B-727-200')
and aircraft.event# = mdd6g1.event#
and aircraft.event# = p8.event# and aircraft.event# = p29.event#
and aircraftweight > 0;
```

Query 2:

```
select aircraft.event#, datetime, aircraftweight, mdd6g1.peak1
from aircraft, mdd6g1, p9, p28
where (aircrafttype = 'B-727' or aircrafttype = 'B-727-200')
and aircraft.event# = mdd6g1.event#
and aircraft.event# = p9.event# and aircraft.event# = p28.event#
and aircraftweight > 0;
```

Similar queries were used to return lists of events for the SDD17 gauge and for the different aircraft groups. The "adjusted" peak deflection for each event was computed using the adjustment factor defined by the formula in equation 1. The adjusted mean peak and 95% confidence limits for the mean were then computed for each of the first three aircraft categories. Confidence limits were not computed for the DC-10 group due to the small number of events for that group.

Table 27 and figures 20 and 21 compare the group means from tables 25 and 26 to the corresponding 3D finite element edge loading solutions. Two finite element cases were considered: (a) zero bond at the slab-base interface (sliding interface) and (b) full bond at the slab-base interface (tied interface). Since the positive displacement direction is taken in the upward direction, a more negative value represents a larger displacement under the load.

TABLE 27. PEAK DEFLECTION COMPARISON (EDGE LOAD CASE)

Aircraft Type	Mean Adjusted Peak Deflection, mils		3D Finite Element Deflection, mils	
	MDD6G1	SDD17	Sliding I/F	Tied I/F
B-727	-13.44	-13.48	-14.86	-11.83
B-737	-9.66	-9.24	-9.92	-7.12
B-757	-19.36	-18.47	-19.00	-14.29
DC-10	-28.32	-26.59	-28.17	-22.07

The following observations were made from figures 20 and 21:

1. Adjusted peak responses of MDD6, gauge 1, and SDD17 varied widely from their respective means. Hence, an individual gauge reading could depart significantly from the computed response, although the mean values were close.

2. The variability of peak deflection readings for the edge case (MDD6 and SDD17) was significantly greater than for the interior case (MDD6).

3. Predicted values of deflection under the wheel path from 3D finite element analysis were generally very close to the DIA mean values. The sliding interface and tied interface cases may be considered upper and lower bounds, respectively, on the predicted deflection.

4. The above results are inconclusive as to whether the sliding interface finite element model is a better overall predictor of slab deflection at DIA than the tied interface model. In most cases, the mean DIA response fell between the two finite element model

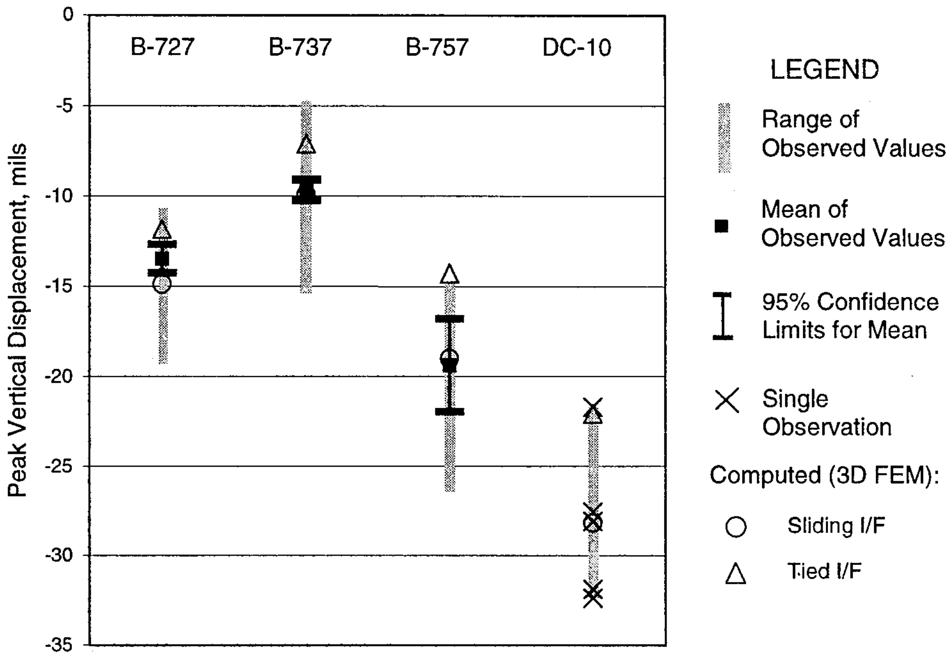

FIGURE 20. PEAK DEFLECTION OF SLAB AT MDD6 (GAUGE 1) COMPARED TO 3D FINITE ELEMENT SOLUTION FOR VARIOUS AIRCRAFT TYPES

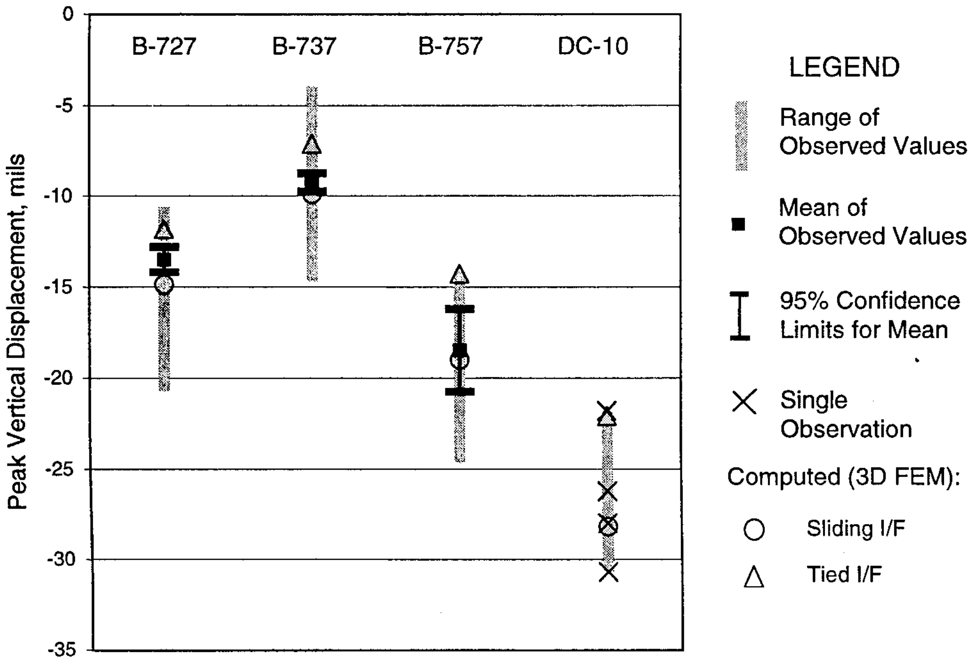

FIGURE 21. PEAK DEFLECTION OF SLAB AT SDD17 COMPARED TO 3D FINITE ELEMENT SOLUTION FOR VARIOUS AIRCRAFT TYPES

predictions, suggesting that the actual condition near the gauge is intermediate between the two extremes (i.e., partial bond). However, in three cases, (B-737, B-757, and DC-10 for MDD6G1), the sliding interface model was able to predict the mean DIA response almost exactly. No case showed significantly better agreement for the tied model.

The higher variability of the deflection response at the slab edge relative to the response at the interior can be explained partly as a consequence of temperature variations. As shown in the following section, the load transfer efficiency of the undoweled dummy joint (i.e., the ability of the dummy joint to transfer part of the load from the loaded to the unloaded slab) is positively correlated to the concrete temperature. As the temperature of the slab increases, deflection of the loaded slab tends to decrease due to the additional increment of support provided by the unloaded slab. Hence, there is a negative correlation between the concrete temperature and the deflection response near the joint. By contrast, there is little temperature effect on the deflection response at the center of the slab. Figure 22 plots the peak (adjusted) deflection response at gauge SDD17 (transverse edge of slab) as a function of the surface temperature of slab B3 for B-737 aircraft. The correlation coefficient for the relation shown in figure 22 is 0.649.

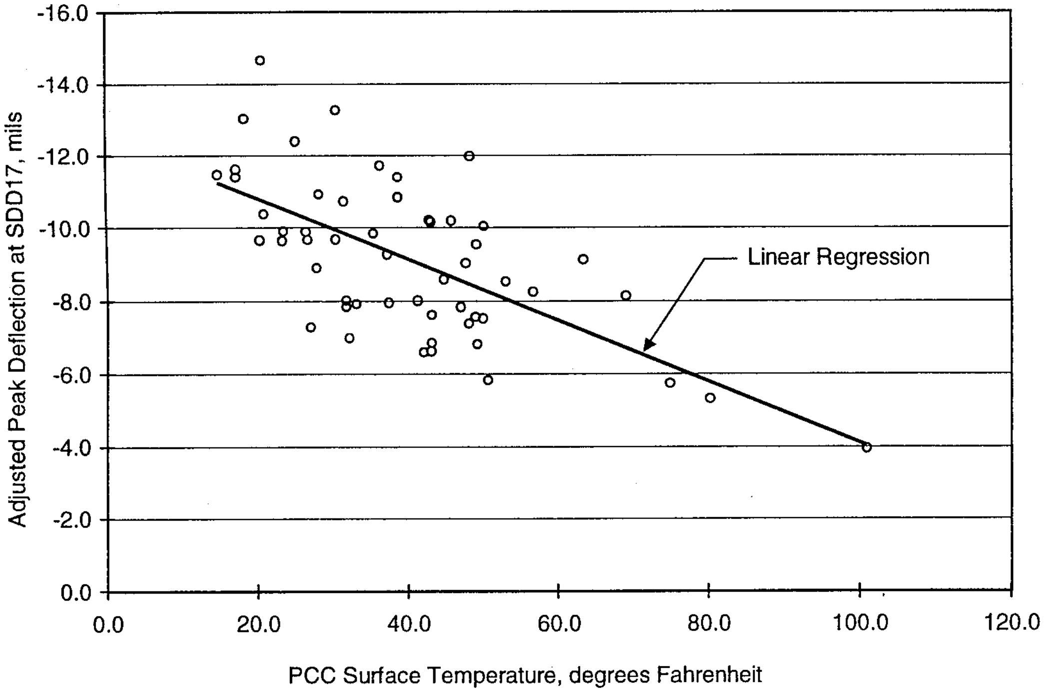

FIGURE 22. CORRELATION BETWEEN PCC SURFACE TEMPERATURE AND ADJUSTED PEAK DEFLECTION RESPONSE AT LVDT SENSOR SDD17 (FOR B-737 EVENTS)

LOAD TRANSFER EFFICIENCY COMPARISONS

Load transfer efficiency in rigid pavements is usually defined as the ratio of a given response in an unloaded slab to the same response in an adjacent slab to which a load is applied. Since load transfer efficiency is calculated from measurements of actual pavement responses (e.g., vertical displacement and strain), it can be used for evaluating joint performance in the field. From a theoretical point of view, the concept of load transfer efficiency needs to be carefully defined

1. The term "efficiency" suggests a property of the pavement/joint structure, independent of external factors. In fact, finite element analysis shows that for a linear elastic joint structure, the computed load transfer efficiency depends on the configuration of the applied load and the number of wheels, as well as on the elastic properties of the joint and the other materials. Therefore, the same joint structure can produce very different values of load transfer efficiency, depending on the type of load applied. In the field, joint efficiencies are usually measured by means of an HWD or other dynamic test, and there is no reason to assume that the load transfer efficiency calculated on the basis of the HWD response necessarily corresponds to the in-service value.

2. Load transfer efficiencies based on measurements of slab deflection are not easily converted to efficiencies based on stress (or strain). Hammons and Ioannides [8] attempted to define such a relation using the dimensionless quantity a/l as a parameter, where a is the radius of a circular load, and l is the radius of relative stiffness of a rigid pavement. However, their solution is based on a Winkler (i.e., infinite) subgrade characterized by a modulus of subgrade reaction k. As such, it ignores shear transfer in the subgrade layers that may contribute significantly to the observed load transfer efficiency. Also, as the slab deflection is much more dependent than the slab stress on finite subgrade depth, their solution may not be applicable to pavements where the actual deflections are less than the predicted values due to finite subgrade depth.

Load transfer efficiencies for DIA runway 34 were calculated based on the dynamic gauge responses to aircraft load events. Hence, they represent the in-service load transfer efficiencies. Mean values of in-service load transfer efficiency were calculated and compared with solutions of the 3D finite element model for different aircraft loads.

DEFLECTION-BASED LOAD TRANSFER EFFICIENCY.

The deflection-based load transfer efficiency compares vertical displacements of the PCC slabs on opposite sides of a joint, when one slab only is subject to a vertical load. Load transfer efficiency is defined by the ratio

$$e_\delta = \frac{\delta_U}{\delta_L} \tag{9}$$

where δ_L is the vertical displacement experienced by the loaded slab, δ_U is the *simultaneous* vertical displacement experienced by an adjacent unloaded slab, and both deflections are measured at the same point along the junction of the two slabs on a line perpendicular to the joint. For dynamic loads, where δ_L and δ_U are both functions of time, the value of δ_L to be used in equation 9 is its peak value. Hence, for a dynamic load, δ_U is taken as the deflection of the unloaded slab concurrent with the peak value of deflection δ_L.

Figure 23 shows the location of the LVDT sensors with respect to the aircraft wheel path. For aircraft in-service loads, it is convenient to compute efficiency based on the peak deflection measured at the transverse joint as the aircraft approaches (or leaves) the transverse joint. Described below are two methods for calculating in-service deflection-based load transfer efficiencies from the LVDT sensor data. As shown by the analysis which follows, both methods give results that are approximately equal when applied to the DIA data.

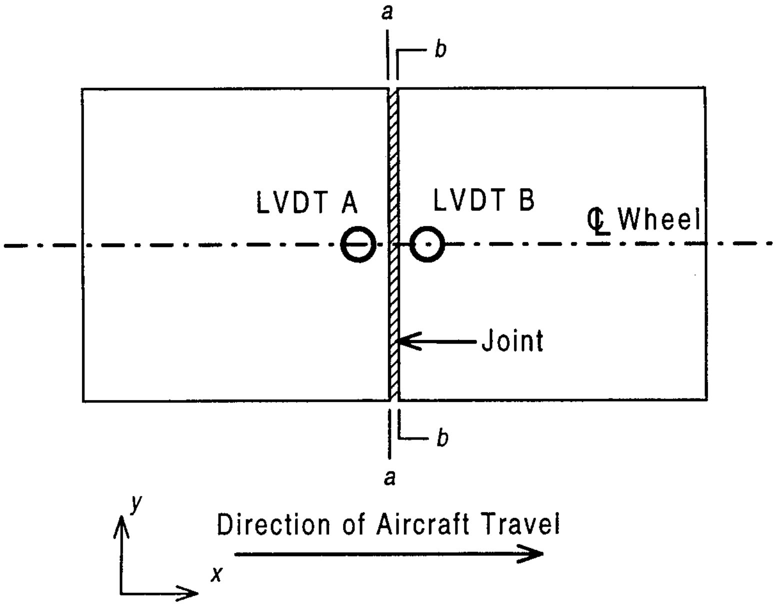

FIGURE 23. TRANSVERSE JOINT INSTRUMENTED WITH LVDT SENSORS

<u>METHOD 1 (DEFLECTION RATIO FROM TWO OPPOSITE SENSORS)</u>. In cases where two LVDT sensors are placed on opposite sides of a joint, data from both sensors can be used to calculate the efficiency ratio. In the case of a transverse joint instrumented as shown in figure 23, assume the movement of the aircraft is in the x direction from A toward B. If the dynamic displacement readings from both sensors are plotted on the same time scale (figure 24), then the joint efficiency can be calculated as

$$e_{\delta}^{(fwd)} = \frac{\delta_a^{(B)}}{\delta_a^{(A)}} \tag{10}$$

in the forward direction or

$$e_{\delta}^{(bak)} = \frac{\delta_b^{(A)}}{\delta_b^{(B)}} \tag{11}$$

in the backward direction, where $\delta_a^{(B)}$ is the displacement response at LVDT B when LVDT A experiences a peak, $\delta_a^{(A)}$ is the peak displacement response at LVDT A, $\delta_b^{(A)}$ is the response at

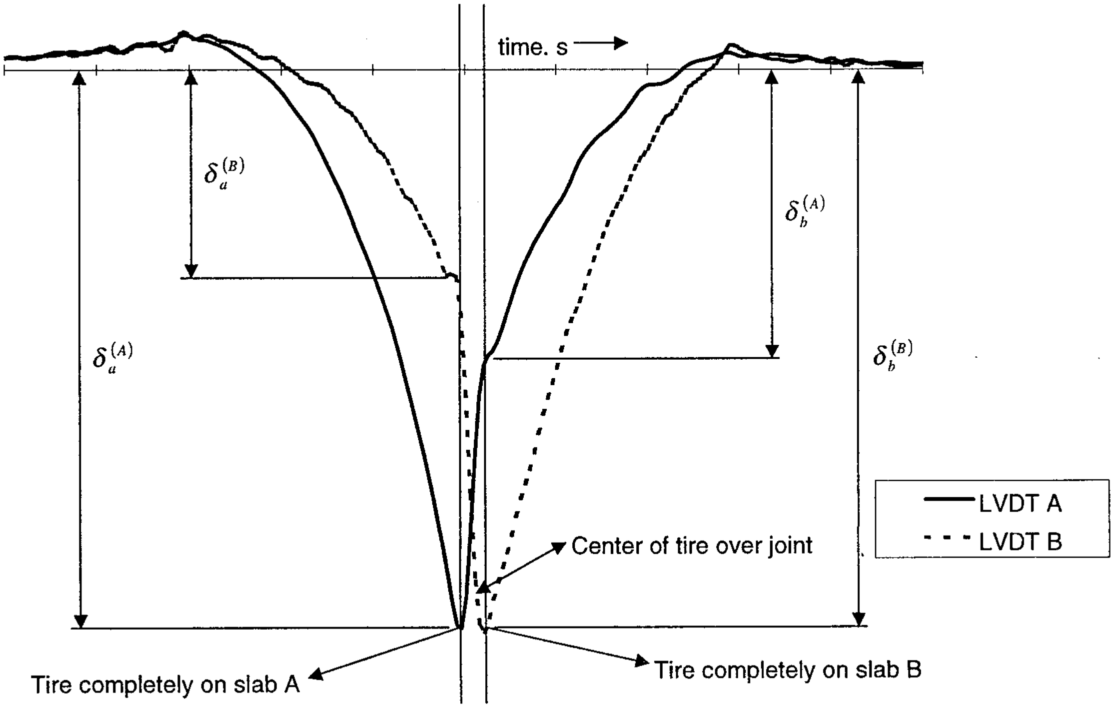

FIGURE 24. CALCULATION OF LOAD TRANSFER EFFICIENCY FROM TWO LVDT SENSORS

LVDT *A* when LVDT *B* experiences a peak, and $\delta_b^{(B)}$ is the peak response at LVDT *B*. The difference in the actual values of e_δ as computed from equation 10 and equation 11 gives an indication of the degree of asymmetry of the joint. The average load transfer efficiency is given by

$$e_\delta^{(avg)} = \frac{1}{2}\left[e_\delta^{(fwd)} + e_\delta^{(bak)}\right]. \tag{12}$$

Disregarding dynamic effects, a symmetrical joint necessarily yields

$$e_\delta^{(fwd)} = e_\delta^{(bak)} = e_\delta^{(avg)} \text{ (symmetrical joint)} \tag{13}$$

METHOD 2 (DEFLECTION RATIO FROM A SINGLE SENSOR). In many cases it is not possible to compute the load transfer efficiency from a pair of sensors recording simultaneously. Simultaneous data may be unavailable in a particular case because one of the two sensors failed to respond, responded with bad data, or because sensors were installed on only one side of the joint in question. However, as long as data is available from a single sensor, relatively accurate estimates of joint efficiency can be obtained by analyzing the shape of the processed signal. A procedure for analyzing the sensor records was developed based on two observations on the general class of dynamic sensor records represented by figure 24. The first observation is that each record exhibits distinct change of slope at a point that closely corresponds in time to the peak reading of the other record. The second observation is that the slope is nearly constant on the segment that connects this point with the peak portion of the curve. From these observations the procedure described below was used to calculate the efficiency. Figure 25 shows a typical data record in which the tire is moving from left to right and the sensor is in the left slab.

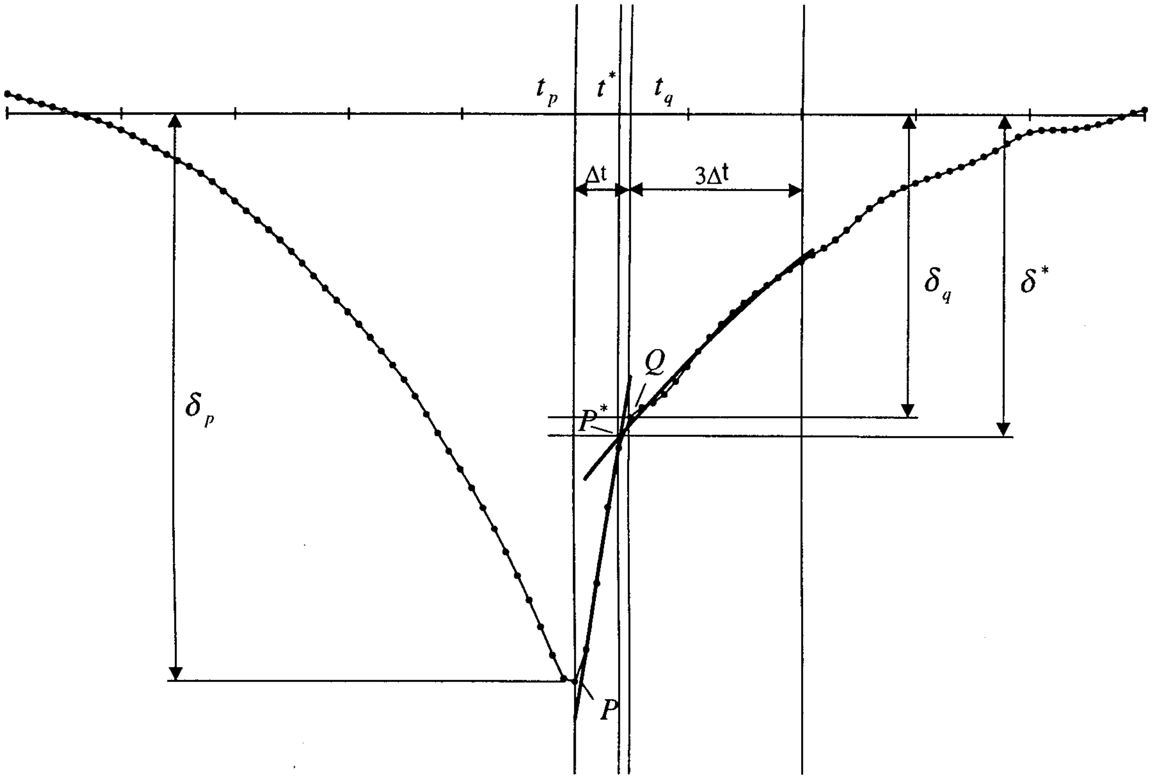

FIGURE 25. CALCULATION OF LOAD TRANSFER EFFICIENCY BY GEOMETRIC METHOD

1. The data point *P* at which the peak value is recorded is identified. The peak coordinates are (t_p, δ_p). This corresponds to the condition where the tire is completely on the left slab containing the sensor, but is just starting to move on to the right slab.

2. The data point *Q* nearest to the point of slope change is identified visually. The coordinates of *Q* are (t_q, δ_q). This corresponds to the condition where the tire is completely on the right slab.

3. The interval $\Delta t = |t_q - t_p|$ is evaluated.

4. For the case where the gauge is located on the leading slab (figure 23), the straight-line best fit to data points in the range $\lfloor t_p + 1, t_q - 1 \rfloor$ is computed. For the case where the

gauge is in the following slab, the straight-line best fit to data points in the range $\lfloor t_q + 1 , t_p - 1 \rfloor$ is computed.

5. For the case where the gauge is located on the leading slab (figure 23), the quadratic best fit to data points in the range $\lfloor t_q , t_q + 3\Delta t \rfloor$ is computed. For the case where the gauge is in the following slab, the quadratic best fit to data points in the range $\lfloor t_q - 3\Delta t , t_q \rfloor$ is computed.

6. The point P^* at which the two curves computed in steps 4 and 5 intersect is computed. Point P^* has coordinates (t^*, δ^*).

7. The load transfer efficiency is estimated as $e_\delta \cong \dfrac{\delta^*}{\delta_p}$.

Except for step 2, which involves a visual judgment, the above procedure can be automated easily. A MATLAB script was written to perform the curve-fitting operations and compute the load transfer efficiency according to the above steps.

In general, method 1 calculations are more "reproducible" than method 2 since the former method does not rely on visual interpretation of the data. Method 2, on the other hand, depends on the correct visual identification of point Q in the processed data record (step 2). Also, for values of e_δ in the upper range ($e_\delta > 0.7$), the location of Q is typically undefined. Therefore, method 2 cannot be used to calculate load transfer efficiency ratios for the upper range of load transfer efficiencies.

In-service deflection-based load transfer efficiencies were computed for the transverse joint between slabs D2 and D3, based on responses of LVDT sensors SDD17 and MDD6 (gauge 1) to aircraft load events. The joint type at this location is type "G" (dummy construction) as shown in figure 10. Unfortunately, it was not possible to calculate LVDT-based load transfer efficiencies for doweled joints (type "D"), due to a lack of LVDT sensors at those joints (figure 2).

In order to compare the two methods of load transfer efficiency calculation, a set of data based on B-727-200 events was analyzed. For this B-727-200 data set, the load transfer efficiencies at the above joint were calculated by both methods, the paired gauge method (method 1) and the single gauge method (method 2). For method 1, the forward and backward load transfer efficiencies were calculated, and the average efficiency was obtained from equation 12. For method 2, single-gauge efficiencies were obtained from SDD17 and MDD6 readings, and the average of the two values was used. For event records where point Q was undefined (see above), $e_\delta^{(avg)} = 0.85$ was assumed. Figure 26 shows the correlation between values of $e_\delta^{(avg)}$ obtained using method 1 (horizontal axis) and method 2 (vertical axis). Each data point represents one B-727-200 event in the time period January 1, 1996 to August 31, 1997. There were a total of 59 events in this data set. As with the peak strain analysis previously discussed, a specific event from the database was included in this data set only if the position sensor data showed that the wheel covered both sensors SDD17 and MDD6. However, unlike the peak strain analysis, events were not necessarily rejected from the data set if the gross aircraft weight was unknown.

The following observations were made from figure 26.

1. There is a very strong correlation between the values of $e_\delta^{(avg)}$ calculated using method 1 and the values for the same events using method 2. The correlation coefficient is 0.995.
2. The linear regression of the data falls nearly along the line of equality.
3. Over the 20-month period in which data was collected, a very wide range of load transfer values was observed. The minimum observed $e_\delta^{(avg)}$ for the data was approximately 0.13. The maximum was approximately 0.85.
4. The assumption of $e_\delta^{(avg)} = 0.85$ for events in the "upper range" (method 2) correlates acceptably well with the values of $e_\delta^{(avg)}$ for these events calculated using method 1.

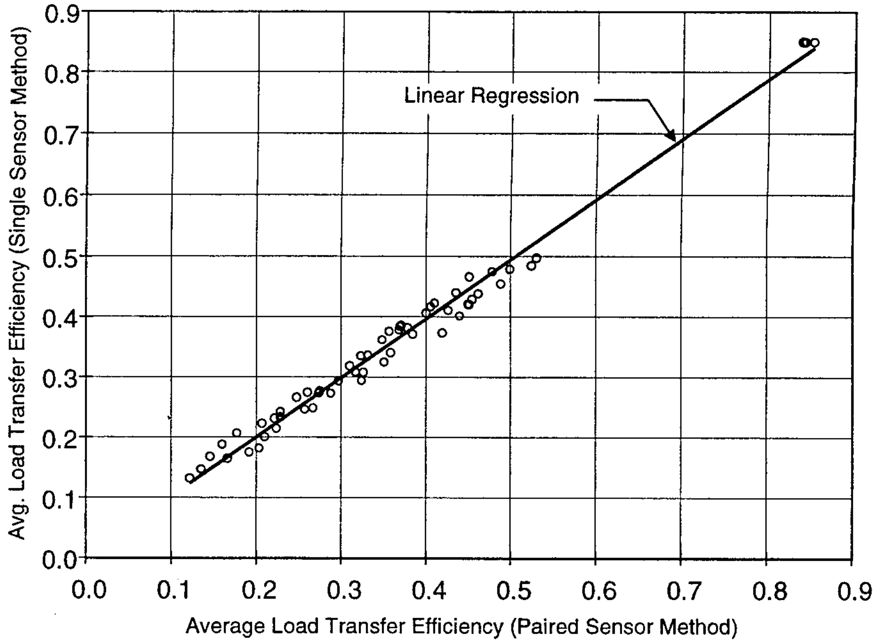

FIGURE 26. CORRELATION OF PAIRED SENSOR (METHOD 1) AND SINGLE SENSOR (METHOD 2) VALUES OF LOAD TRANSFER EFFICIENCY $e_\delta^{(avg)}$

The wide range of observed $e_\delta^{(avg)}$ values may be attributed in part to temperature changes during the period of observation. Temperature changes cause thermal expansion and contraction of the concrete slabs, which in turn affects the degree of aggregate interlock achieved at the joint. In figure 27, the average load transfer efficiency for 57 B-727 events is plotted versus the recorded temperature at the surface of slab B3 (thermistor gauge STEMPB3). The calculated values of

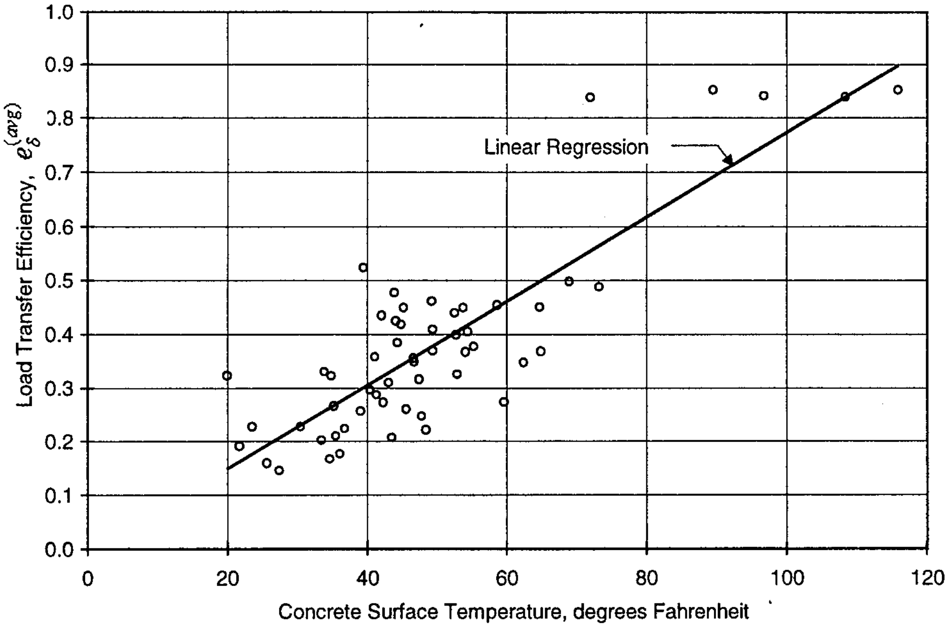

FIGURE 27. OBSERVED LOAD TRANSFER EFFICIENCY $e_\delta^{(avg)}$ AT SDD17 AND MDD6 AS A FUNCTION OF CONCRETE TEMPERATURE (B-727 EVENTS)

$e_\delta^{(avg)}$ are based on two LVDT sensors, SDD17 and MDD6 (gauge 1). Although slab C3 is closer to the LVDT site than slab B3, the temperature variation in slab B3 was used as the independent variable in figure 27 because a significant number of temperature data files for slab C3 were corrupted. Nevertheless, the temperature recorded at thermistor gauge STEMPB3 should closely correspond to the actual slab surface temperature at the LVDT site.

The following observations were made from figure 27.

1. There is a moderately strong correlation between $e_\delta^{(avg)}$ and concrete temperature. Overall, the correlation coefficient is 0.851. However, if the five summer observations are removed, the correlation coefficient for the remaining 52 observations (all winter months) is only 0.629, indicating a significantly weaker correlation between the observed load transfer efficiency and the actual concrete temperature in cold weather.

2. There appear to be two distinct load transfer efficiency regimes, one for winter (in the 0.15-0.55 range) and one for summer. The latter is nearly constant at approximately 0.85.

3. The analysis is handicapped by the lack of data for fall and spring months, when load transfer efficiencies might be expected to fall into an intermediate range (0.55 - 0.85).

Data from sensors SDD17 and MDD6 were used to calculate the mean values of load transfer efficiency $e_\delta^{(avg)}$ for the following aircraft types at DIA: B-727, B-737, B-757, and DC-10. In figure 28, the mean values for winter and summer are compared to the computed values of load transfer efficiency for the same aircraft load using the 3D finite element model. Separate ranges are shown for the winter months (December, January, and February) and the summer months (June, July, and August). The finite element load transfer efficiency was computed as the ratio

$$e_{\delta}^{FEA} = \frac{\delta_{U}^{(static)}}{\delta_{L}^{(static)}} \tag{14}$$

where $\delta_{L}^{(static)}$ is the (static) deflection of the loaded slab at the point where the tire is just touching the unloaded slab, (if the center line is on the joint, then the two slabs are equally loaded), and $\delta_{U}^{(static)}$ is the corresponding (static) deflection of the unloaded slab. The material properties used for the finite element analysis are listed in table 1.

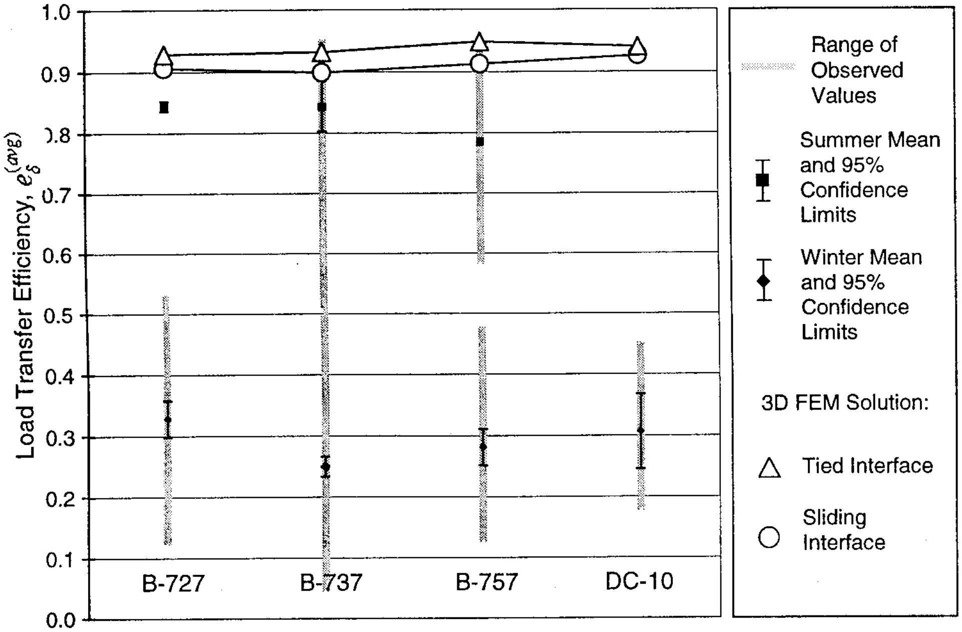

FIGURE 28. LOAD TRANSFER EFFICIENCY $e_{\delta}^{(avg)}$ AT LVDT SENSORS SDD17/MDD6 (METHOD 1) COMPARED TO FINITE ELEMENT SOLUTIONS FOR VARIOUS AIRCRAFT TYPES

The following observations were made from figure 28.

1. The in-service load transfer efficiency varies through a very wide range. Values of $e_{\delta}^{(avg)}$ ranging from less than 0.05 to in excess of 0.95 were observed for the same joint location and the same aircraft load (B-737) at different times of the year.

2. Very low values of $e_{\delta}^{(avg)}$ were observed for the winter months of December, January, and February. From figure 28, the calculated value of $e_{\delta}^{(avg)}$ did not exceed 0.54 for any

individual aircraft event during the winter season. The winter mean values ranged from 0.25 for the B-737 group to 0.38 for the B-727 group.

3. In contrast with the low values of $e_\delta^{(avg)}$ for winter loadings, the summer values were much higher. For both the dual-wheel gears, B-727 and B-737, the mean value of $e_\delta^{(avg)}$ for June, July, and August was approximately 0.85 (with little variance in the case of the B-727). For the dual-tandem B-757, the mean observed $e_\delta^{(avg)}$ was somewhat lower. (No usable summer events involving the DC-10 aircraft were found in the database). Differences should be expected due to the different gear configurations (tire contact patch lengths, dual and tandem spacings, and dual versus dual-tandem).

4. Values of load transfer efficiency predicted by the 3D finite element model $e_\delta^{(FEA)}$ exceed 0.90 for all aircraft groups. Since the finite element model assumes significant load transfer at the joint (k_{jnt} = 100,000 lbs/in^2 (690 MPa)), the finite element solution should be compared to field observations made during the summer, when higher concrete temperatures result in higher effective load transfer efficiencies. Figure 28 shows that even if only the summer events are considered, the model prediction of deflection-based load transfer efficiency is significantly higher than the DIA mean in-service value.

ANALYSIS OF VARIANCE (ANOVA). Figure 28 shows significant differences in the mean load transfer efficiency $e_\delta^{(avg)}$ for different aircraft groups, for example, between the B-727 and B-737 winter means. In order to determine the relative contribution of group-based differences to the total variation, ANOVA was performed on the total data set. The results of this analysis are presented in tables 28 and 29. ANOVA confirms that, for the winter data, the differences between groups (i.e., between group means) are statistically significant at the 5% significance level. By contrast, ANOVA shows that differences between groups of aircraft are not significant for the summer data (at the 5% level).

TABLE 28a. GROUP DATA SUMMARY FOR ANOVA OF DEFLECTION-BASED LOAD TRANSFER EFFICIENCY FOR EVENTS IN WINTER

Groups	Count	Sum	Mean $e_\delta^{(avg)}$	Variance
B-727	54	17.71581	0.328071	0.011924
B-737	180	45.0027	0.250015	0.012415
B-757	44	12.36307	0.280979	0.00949
DC-10	14	4.291657	0.306547	0.011084

TABLE 28b. ANOVA OF DEFLECTION-BASED LOAD TRANSFER EFFICIENCY FOR EVENTS IN WINTER

Source of Variation	SS	df	MS	F	P-value	F crit
Between Groups	0.277019	3	0.09234	7.807053	5E-05	2.63595
Within Groups	3.406387	288	0.011828			
Total	3.683406	291				

TABLE 29a. GROUP DATA SUMMARY FOR ANOVA OF DEFLECTION-BASED LOAD TRANSFER EFFICIENCY FOR EVENTS IN SUMMER

Groups	Count	Sum	Mean $e_\delta^{(avg)}$	Variance
B-727	5	4.224033	0.844807	0.000045
B-737	27	22.7877	0.843989	0.010789
B-757	6	4.686955	0.781159	0.0293
DC-10	0	-	-	-

TABLE 29b. ANOVA OF DEFLECTION-BASED LOAD TRANSFER EFFICIENCY FOR EVENTS IN SUMMER

Source of Variation	SS	df	MS	F	P-value	F crit
Between Groups	0.02003	2	0.010015	0.820532	0.448487	3.267417
Within Groups	0.427187	35	0.012205			
Total	0.447217	37				

STRAIN-BASED LOAD TRANSFER EFFICIENCY.

The strain-based load transfer efficiency is calculated as the ratio of strain in the unloaded slab to strain in the loaded slab:

$$e_\varepsilon = \frac{\varepsilon_U}{\varepsilon_L} \tag{15}$$

where ε_L is the tensile strain at the extreme fibers of the loaded slab, ε_U is the *simultaneous* tensile strain at the extreme fibers of the adjacent unloaded slab, and both strains are measured at the same horizontal location along the junction of the two slabs. Rollings [9] uses the term "load transfer" to refer to the quantity in equation 15, while reserving the expression "joint efficiency" for the deflection ratio defined by equation 9. However, load transfer also refers to a related quantity, namely, the ratio of maximum stress in the jointed slab to the maximum stress that would occur in a slab with a free edge. Hence, it is important to define the terms that are used carefully. For dynamic loads, where ε_L and ε_U are both functions of time, the value of ε_L to be used in equation 15 is its peak value. For a dynamic load, ε_U in equation 15 is defined as the strain in the bottom fiber of the unloaded slab concurrent with the peak value of strain ε_L.

For the in-service load transfer efficiency, the values of ε_L and ε_U in equation 15 are obtained from H-bar strain gauge data. The computation of e_ε from H-bar readings is analogous to the computation of e_δ from LVDT data. As with the latter, the former can be obtained either from geometric analysis of a single sensor located near the edge of the slab or from a pair of sensors on opposite sides of a joint.

METHOD 1 (STRAIN RATIO FROM TWO OPPOSITE SENSORS). If a pair of H-bar sensors is used to compute in-service e_ε values, as illustrated in figure 29, then an additional adjustment to the data is needed to compensate for the difference in the vertical position of the two gauges. Otherwise, the calculation procedure is described by equations 10 through 12, with strain values $\varepsilon_a^{(A)}, \varepsilon_a^{(B)}, \varepsilon_b^{(A)}$, and $\varepsilon_b^{(B)}$ replacing deflections $\delta_a^{(A)}, \delta_a^{(B)}, \delta_b^{(A)}$, and $\delta_b^{(B)}$, respectively, and with $e_\varepsilon^{(fwd)}, e_\varepsilon^{(bak)}$, and $e_\varepsilon^{(avg)}$ replacing the quantities $e_\delta^{(fwd)}, e_\delta^{(bak)}$, and $e_\delta^{(avg)}$, respectively, in the appropriate equations. Defining t_a as the time when strain gauge A experiences its peak response and t_b as the time when strain gauge B experiences its peak response, the additional data adjustment is provided by the following equations:

$$\varepsilon_a^{(A)} = \hat{\varepsilon}_a^{(A)} + s_a^{(A)}(d_B - d_A) \tag{16}$$

$$\varepsilon_b^{(A)} = \hat{\varepsilon}_b^{(A)} + s_b^{(A)}(d_B - d_A) \tag{17}$$

where $\hat{\varepsilon}_a^{(A)}$ and $\hat{\varepsilon}_b^{(A)}$ are the unadjusted readings at strain gauge A at, respectively, times t_a and t_b; $s_a^{(A)}$ is the slope of the (linear) strain distribution through the thickness of the slab at gauge A at time t_a; $s_b^{(A)}$ is the slope of the strain distribution at gauge A at time t_b; d_A is the depth of embedment of strain gauge A measured from the top of the slab; and d_B is the depth of embedment of strain gauge B measured from the top of the slab. If $d_A = d_B$, then equations 16 and 17 reduce to $\varepsilon_a^{(A)} = \hat{\varepsilon}_a^{(A)}$ and $\varepsilon_b^{(A)} = \hat{\varepsilon}_b^{(A)}$, i.e., the calculation is no different than for deflection-based load transfer efficiency. The above equations assume that both slabs have approximately the same thickness near the joint. Errors resulting from minor differences in slab thickness are small and can be neglected.

In equations 16 and 17, the slopes $s_a^{(A)}$ and $s_b^{(A)}$ of the strain distribution needs to be computed. If it is assumed that the neutral axis coincides with the mid-plane of the slab, then the slopes are calculated as

$$s_a^{(A)} = \frac{\hat{\varepsilon}_a^{(A)}}{d_A - 0.5h_A} \tag{18}$$

$$s_b^{(A)} = \frac{\hat{\varepsilon}_b^{(A)}}{d_A - 0.5h_A} \tag{19}$$

where h_A is the slab thickness in the vicinity of strain gauge A. However, the assumption that the neutral axis is located at mid-plane may not be accurate, particularly if bonding between the slab and the first base course is significant. In that case, the neutral axis is located below mid-plane, and equations 18 and 19 should not be used. If strain gauges are located near the top and the bottom of the slab (see figure 29), then accurate estimates of the slopes of the strain distributions can be obtained from

$$s_a^{(A)} = \frac{\hat{\varepsilon}_a^{(A)} - \hat{\varepsilon}_a^{(C)}}{d_A - d_C} \tag{20}$$

$$s_b^{(A)} = \frac{\hat{\varepsilon}_b^{(A)} - \hat{\varepsilon}_b^{(C)}}{d_A - d_C} \tag{21}$$

where $\hat{\varepsilon}_a^{(C)}$ and $\hat{\varepsilon}_b^{(C)}$ are the recorded (compressive) strains at strain gauge C in figure 29 at times t_a and t_b respectively, and d_C is the embedment depth of gauge C measured from the top of the slab.

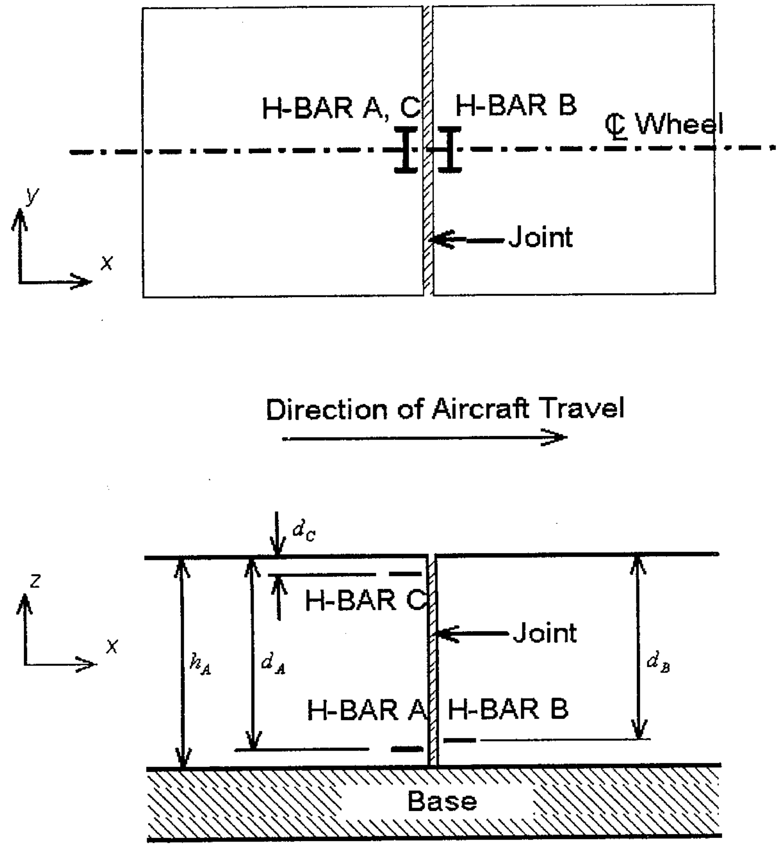

FIGURE 29. TRANSVERSE JOINT INSTRUMENTED WITH H-BAR SENSORS

In equations 16 through 21, tensile strains are positive and compressive strains are negative. In figure 29, gauges A and B are depicted as recording positive (tensile) strains at the bottom of the slab, and gauge C as recording negative (compressive) strains at the top. However, it should be noted that the above equations equally apply to the opposite situation, i.e., where A and B are at the top of the slab and C is located at the bottom, below A.

METHOD 2 (STRAIN RATIO FROM A SINGLE SENSOR). In cases where the strain ratio cannot be computed from dual sensors, it is possible to compute the strain-based load efficiency from geometric analysis of a single H-bar sensor reading. The procedure follows steps 1 through 6 on pages 39 and 40, except that the deflection values δ_p, δ_q, and δ^* are replaced by the corresponding strain values $\varepsilon_p, \varepsilon_q$, and ε^*, as appropriate.

Strain-based load transfer efficiencies were calculated from DIA H-bar data for two transverse joints, a type G (dummy construction) joint and a type D (doweled) joint. The type G joint is located on the north side of slab D2 (south side of slab D3). Method 1 was used to calculate the strain ratios for this joint based on readings from paired H-bar strain gauges H42 (top of slab D2) and H13 (top of slab D3). The arrangement of strain gauges at the dummy joint is shown in figure 30(a). The type D (doweled) joint is located on the north side of slab D4, as shown in figure 30(b). Instrumentation was not installed on the north side of the doweled joint. Hence, method 2 was used. Strain gauges H26 (bottom of slab) and H45 (top of slab) provided in-service strain data for the method 2 calculation.

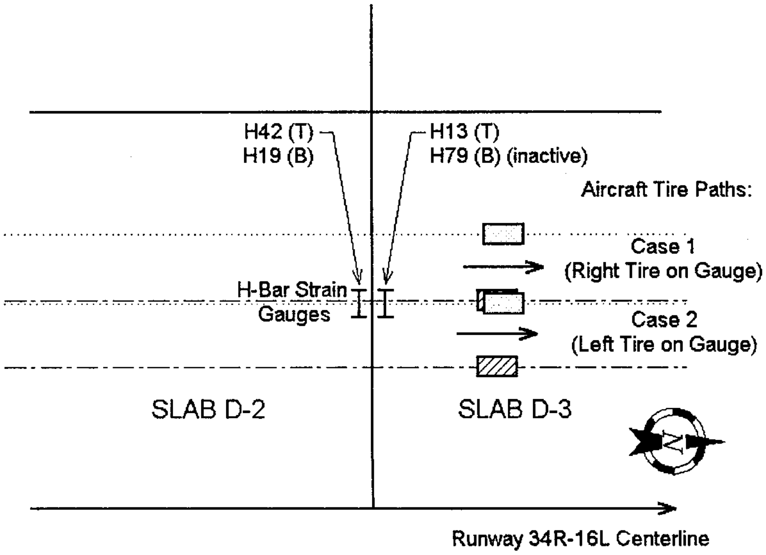

(a) Dummy Transverse Joint

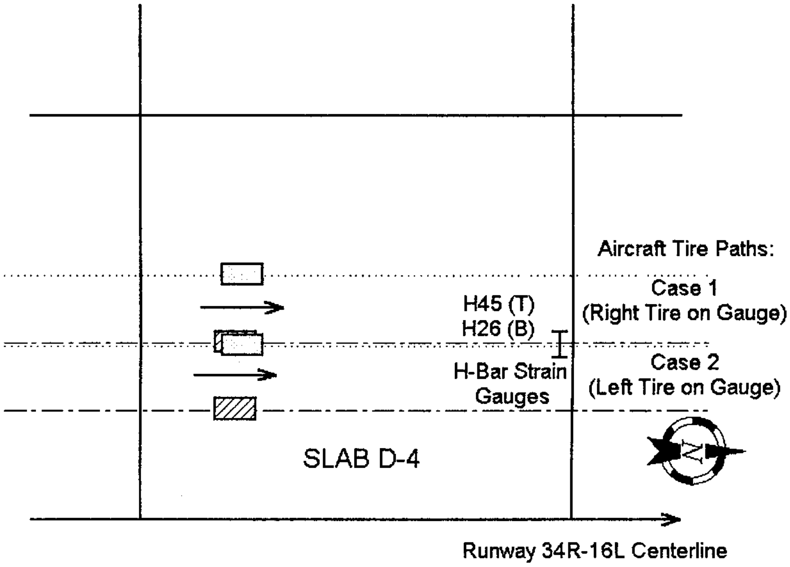

(b) Doweled Transverse Joint

FIGURE 30. STRAIN GAUGE COVERAGE FOR EDGE LOAD CASE

Figures 30(a) and (b) illustrate the two possible paths of aircraft tires crossing the gauge. In case 1 the right aircraft tire covers the gauge, and in case 2 the left aircraft tire covers the gauge. For purposes of statistical analysis, no distinction was made between the responses for right tire coverage and left tire coverage. As in the previous analyses involving peak strain and peak deflection, the position (P) sensor responses were used to establish coverage of the strain gauge by either aircraft tire for a particular aircraft event.

EFFICIENCY OF DUMMY JOINT. Mean values of load transfer efficiency for the undoweled (dummy construction) joint were calculated by method 1 based on the responses of strain gauges H13 and H42. In-service efficiencies based on H-bar strain responses were calculated for two time periods (January/February 1996 and July/August 1997) and for five aircraft categories (B-727, B-737, B-757, DC-10, and B-777). Due to insufficient data, mean values could not be calculated for all the aircraft types for both time periods. An event summary is given in table 30.

TABLE 30. EVENT SUMMARY FOR LOAD TRANSFER EVENTS AT STRAIN GAUGES H13 AND H42 (UNDOWELED JOINT)

	Number of Events, *n*		
Aircraft Category	Jan./Feb. 1996	Jul./Aug. 1997	Total
B-727 (-200)	93	13	106
B-737 (-100, -200, -300, -400, -500)	264	20	284
B-757 (-200)	26	4	30
DC-10	2	0	2
B-777	0	1	1

Based on strain gauge readings, load transfer efficiencies were calculated for both the forward and backward directions. The forward direction is defined with reference to the direction of aircraft travel shown in figure 30. Hence, for the present case, H42 corresponds to strain gauge A, H13 to strain gauge B, and H19 to strain gauge C, in equations 18 through 21. Tables 31 through 34 present summary statistics for load transfer efficiency in the forward and reverse directions for the two time periods (January/February 1996 and July/August 1997). For the time period January/February 1996, significant differences are noted between load transfer efficiency values in the forward and reverse directions, due to asymmetry of the dummy joint. Similar differences are not noted for the time period July/August 1997.

TABLE 31. SUMMARY STATISTICS FOR LOAD TRANSFER EFFICIENCY IN THE FORWARD DIRECTION FROM STRAIN GAUGES H13 AND H42 (JANUARY/FEBRUARY 1996)

Aircraft Type	Count *n*	Load Transfer Efficiency Statistics				
		Sample Mean	Sample Variance	Range of Observed Values		95% Confidence Limits for Mean (±)
				Limit	±	
B-727	93	0.0458	0.001428	-0.049	0.1112	0.0078
B-737	264	0.0168	0.001447	-0.074	851.54	0.0046
B-757	26	0.0590	0.001957	-0.026	0.0916	0.0179
DC-10	2	0.1560	-	0.0976	0.0584	-
B-777	0	-	-	-	-	-

TABLE 32. SUMMARY STATISTICS FOR LOAD TRANSFER EFFICIENCY IN THE BACKWARD DIRECTION FROM STRAIN GAUGES H13 AND H42 (JANUARY/FEBRUARY 1996)

Aircraft Type	Count *n*	Load Transfer Efficiency Statistics				
		Sample Mean	Sample Variance	Range of Observed Values		95% Confidence Limits for Mean (±)
				Limit	±	
B-727	93	0.3332	0.003740	0.1791	0.1478	0.1569
B-737	264	0.2823	0.005529	0.1134	0.1878	0.0091
B-757	26	0.3439	0.007158	0.2172	0.145	0.0342
DC-10	2	0.3702	-	0.3265	0.0437	
B-777	0	-	-			

TABLE 33. SUMMARY STATISTICS FOR LOAD TRANSFER EFFICIENCY IN THE FORWARD DIRECTION FROM STRAIN GAUGES H13 AND H42 (JULY/AUGUST 1997)

Aircraft Type	Count *n*	Load Transfer Efficiency Statistics				
		Sample Mean	Sample Variance	Range of Observed Values		95% Confidence Limits for Mean (±)
				Limit	±	
B-727	13	0.4353	0.025234	0.2699	0.2416	0.096
B-737	20	0.4193	0.035620	0.198	0.3364	0.0883
B-757	4	0.5436	-	0.3345	0.2168	-
DC-10	0	-	-	-	-	-
B-777	1	0.4286	-	-	-	-

TABLE 34. SUMMARY STATISTICS FOR LOAD TRANSFER EFFICIENCY IN THE BACKWARD DIRECTION FROM STRAIN GAUGES H13 AND H42 (JULY/AUGUST 1997)

Aircraft Type	Count *n*	Load Transfer Efficiency Statistics				
		Sample Mean	Sample Variance	Range of Observed Values		95% Confidence Limits for Mean (±)
				Limit	±	
B-727	13	0.4666	0.023464	0.2359	0.2168	0.0926
B-737	20	0.4621	0.029232	0.2515	0.3035	0.0801
B-757	4	0.4714	-	0.3036	0.1718	-
DC-10	0	-	-	-	-	-
B-777	1	0.4498	-	-	-	-

In figures 31 and 32, the computed values of strain-based load transfer efficiency from 3D finite element analysis (assuming the default joint spring constant of 100,000 lbs/in^2 (690 MPa)) are plotted next to the mean field values from tables 31 through 34 (average of forward and backward values). As in the previous comparisons, two sets of finite element solutions are plotted: (a) for the case assuming fully bonded conditions at the slab-base interface and (b) for the case assuming fully unbonded conditions (slip) at the slab-base interface. In this way, the effect of the interface bond strength on the finite element solution can be assessed. (The load transfer efficiency from finite element analysis was taken as the ratio of maximum strain in the unloaded slab to maximum strain in the loaded slab (where both strains are transverse strains and both are evaluated along the tire centerline)). However, the value of this ratio is not constant through the thickness of the slab and depends on the depth at which it is evaluated. The plotted values in figures 31 and 32 for computed load transfer efficiency are the values computed at the H13 depth.

From an examination of figures 31 and 32 for the dummy joints, the following observations can be made.

1. There is a significant difference in the measured load transfer efficiency of the dummy joint between the winter and summer time periods. For the winter time period (figure 32), the mean in-service load transfer efficiency for the joint fell between 0.15 and 0.2, and the maximum observed load transfer efficiency for any event was 0.31. By contrast, for the summer time period (figure 31), the efficiency ranged from 0.25 to as high as 0.87, and calculated mean values for the dual-wheel aircraft gears were approximately 0.45. The much higher load transfer observed in the summer is attributable to higher aggregate interlock due to expansion of concrete in the warmer weather.
2. The computed values of strain-based load transfer efficiency from the 3D finite element model are comparable to the observed mean values for summer events (figure 31) but are much higher than the corresponding mean values for winter events (figure 32).
3. The loading aircraft type did not have a major effect on the computed values of load transfer efficiency.
4. The assumed bond strength (fully bonded versus unbonded) did not have a major effect on the computed values of load transfer efficiency.

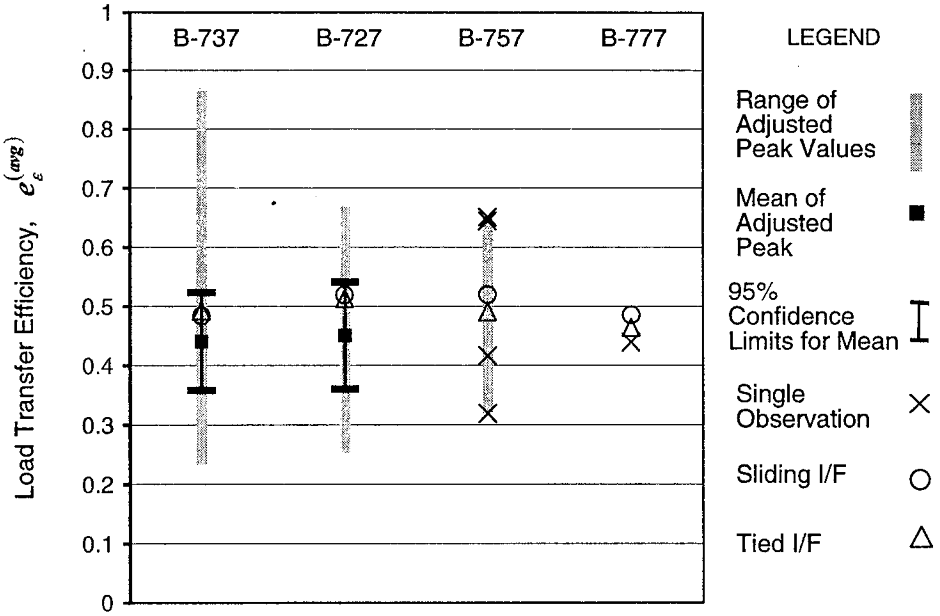

FIGURE 31. STRAIN-BASED LOAD TRANSFER EFFICIENCY $e_\varepsilon^{(avg)}$ AT H-BAR STRAIN GAUGES H19/H42 (METHOD 1) COMPARED TO 3D FINITE ELEMENT SOLUTIONS (DATA FROM JULY/AUGUST 1997)

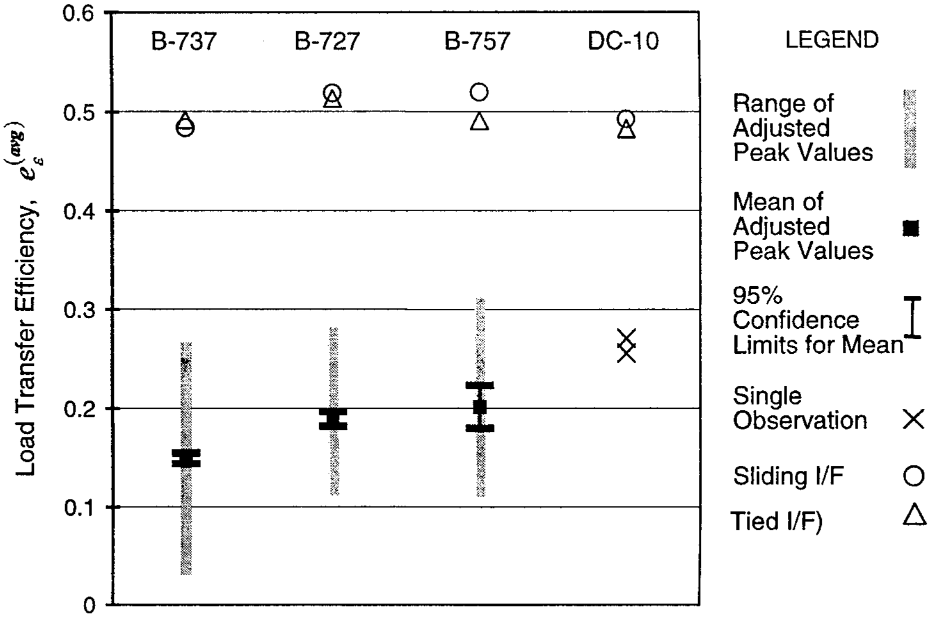

FIGURE 32. STRAIN-BASED LOAD TRANSFER EFFICIENCY $e_\varepsilon^{(avg)}$ AT H-BAR STRAIN GAUGES H19/H42 (METHOD 1) COMPARED TO 3D FINITE ELEMENT SOLUTIONS (DATA FROM JANUARY/FEBRUARY 1996)

EFFICIENCY OF DOWELED JOINT. Mean values of load transfer efficiency for the doweled joint were calculated by method 2 based on the responses of strain gauges H26 and H45. In-service efficiencies based on H-bar strain responses were calculated for three time periods (January/February 1996, November/December 1996, and July/August 1997) and for five aircraft categories (B-737-100, B-737-200, MD-82/88, B-727-200, and B-757). Due to insufficient data, mean values could not be calculated for all the aircraft types for all three of the time periods. An event summary is given in table 35.

TABLE 35. EVENT SUMMARY FOR LOAD TRANSFER EVENTS AT STRAIN GAUGES H26 AND H45 (DOWELED JOINT)

Aircraft Category	Number of Events, *n*			
	Jan./Feb. 1996	Nov./Dec. 1996	Jul./Aug. 1997	Total
B-737-100	27	10	8	45
B-737-200	55	23	10	88
MD-82/88	16	3	1	20
B-727-200	59	26	13	98
B-757	10	0	3	13

Tables 36 through 41 present summary statistics for load transfer efficiency for the three time periods (January/February 1996, November/December 1996, and July/August 1997). In figures 33 through 38, the computed values of stress-based load transfer efficiency from 3D finite element analysis are plotted next to the mean field values from tables 36 through 41. As in the previous comparisons, two sets of finite element solutions are plotted: (a) for the case assuming fully bonded conditions at the slab-base layer interface and (b) for the case assuming fully unbonded conditions (slip) at the slab-base interface. In this way, the effect of the interface bond strength can be assessed.

TABLE 36. SUMMARY STATISTICS FOR LOAD TRANSFER EFFICIENCY BASED ON STRAIN GAUGE H26 (JANUARY/FEBRUARY 1996)

Aircraft Type	Count *n*	Load Transfer Efficiency Statistics				
		Sample Mean	Sample Variance	Range of Observed Values		95% Confidence Limits for Mean (±)
				Limit	±	
B-737-100	27	0.17723	0.001837	0.1869	0.095	0.017
B-737-200	55	0.18340	0.003053	0.1901	0.1071	0.0149
MD-82/88	16	0.21227	0.001367	0.2091	0.0693	0.0197
B-727-200	59	0.22604	0.004336	0.2701	0.1544	0.0172
B-757	10	0.23256	0.004382	0.2591	0.1072	0.0474

TABLE 37. SUMMARY STATISTICS FOR LOAD TRANSFER EFFICIENCY BASED ON STRAIN GAUGE H45 (JANUARY/FEBRUARY 1996)

Aircraft Type	Count *n*	Load Transfer Efficiency Statistics				
		Sample Mean	Sample Variance	Range of Observed Values		95% Confidence Limits for Mean (±)
				Limit	±	
B-737-100	27	0.12789	0.001688	0.1319	0.0851	0.0163
B-737-200	55	0.13845	0.001853	0.1292	0.1039	0.0117
MD-82/88	16	0.16175	0.001619	0.1553	0.065	0.0215
B-727-200	59	0.18926	0.002373	0.1992	0.0963	0.0127
B-757	10	0.20503	0.002342	0.225	0.0726	0.0346

TABLE 38. SUMMARY STATISTICS FOR LOAD TRANSFER EFFICIENCY BASED ON STRAIN GAUGE H26 (NOVEMBER/DECEMBER 1996)

Aircraft Type	Count *n*	Load Transfer Efficiency Statistics				
		Sample Mean	Sample Variance	Range of Observed Values		95% Confidence Limits for Mean (±)
				Limit	±	
B-737-100	10	0.17749	0.000967	0.1748	0.0486	0.0921
B-737-200	23	0.15978	0.000931	0.1511	0.0615	0.0132
MD-82/88	3	-	-	0.1766	0.033	-
B-727-200	26	0.18047	0.002769	0.2023	0.0874	0.0213
B-757	0	-	-	-	-	-

TABLE 39. SUMMARY STATISTICS FOR LOAD TRANSFER EFFICIENCY BASED ON STRAIN GAUGE H45 (NOVEMBER/DECEMBER 1996)

Aircraft Type	Count *n*	Load Transfer Efficiency Statistics				
		Sample Mean	Sample Variance	Range of Observed Values		95% Confidence Limits for Mean (±)
				Limit	±	
B-737-100	10	0.14958	0.001055	0.1571	0.0529	0.0233
B-737-200	23	0.14787	0.000767	0.1679	0.0633	0.012
MD-82/88	3	-	-	0.1637	0.0181	-
B-727-200	26	0.17365	0.001482	0.186	0.0702	0.0156
B-757	0	-	-	-	-	-

TABLE 40. SUMMARY STATISTICS FOR LOAD TRANSFER EFFICIENCY BASED ON STRAIN GAUGE H26 (JULY/AUGUST 1997)

Aircraft Type	Count *n*	Load Transfer Efficiency Statistics				
		Sample Mean	Sample Variance	Range of Observed Values		95% Confidence Limits for Mean (±)
				Limit	±	
B-737-100	8	0.65239	0.045294	0.6681	0.2991	0.1779
B-737-200	10	0.61332	0.038819	0.6194	0.328	0.141
MD-82/88	1	-	-	-	-	-
B-727-200	13	0.46861	0.018619	0.4936	0.201	0.0825
B-757	3	-	-	0.5412	0.0269	-

TABLE 41. SUMMARY STATISTICS FOR LOAD TRANSFER EFFICIENCY BASED ON STRAIN GAUGE H45 (JULY/AUGUST 1997)

Aircraft Type	Count *n*	Load Transfer Efficiency Statistics				
		Sample Mean	Sample Variance	Range of Observed Values		95% Confidence Limits for Mean (±)
				Limit	±	
B-737-100	8	0.60901	0.025191	0.5091	0.2228	0.1327
B-737-200	10	0.51875	0.018594	0.5001	0.2366	0.2476
MD-82/88	1	-	-	-	-	-
B-727-200	13	0.42908	0.018325	0.4739	0.2208	0.0818
B-757	3	-	-	0.5474	0.1188	-

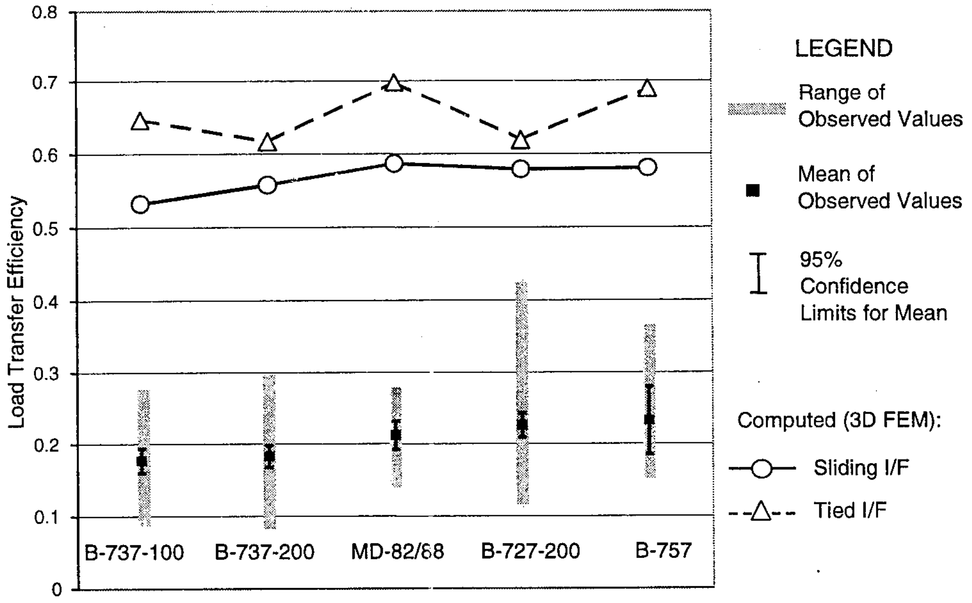

FIGURE 33. STRAIN-BASED LOAD TRANSFER EFFICIENCY e_ε AT H-BAR STRAIN GAUGE H26 (METHOD 2) COMPARED TO 3D FINITE ELEMENT SOLUTIONS (DATA FROM JANUARY/FEBRUARY 1996)

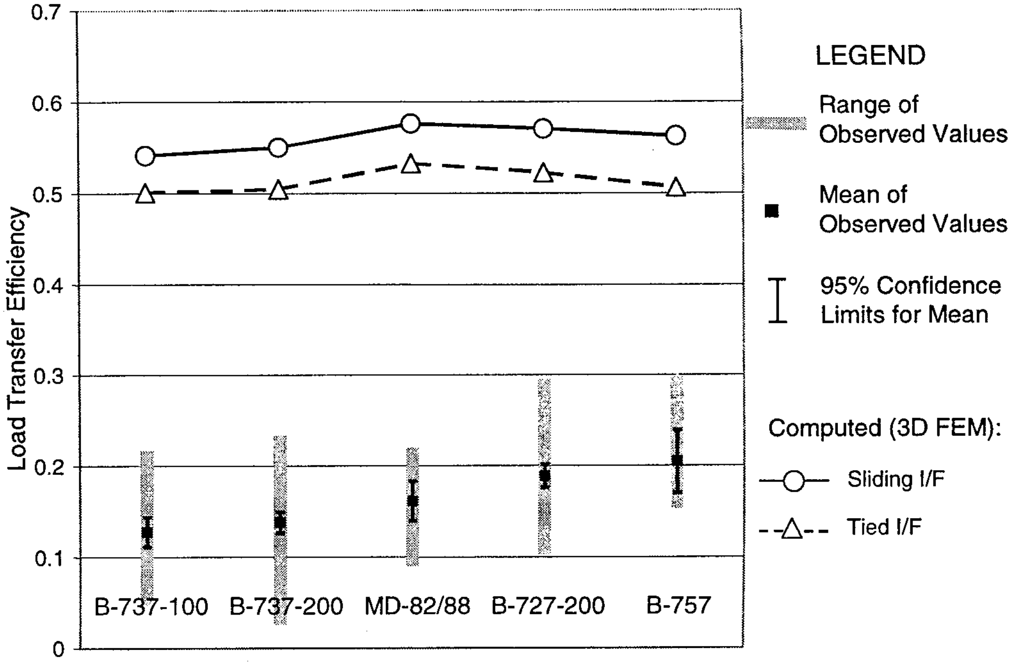

FIGURE 34. STRAIN-BASED LOAD TRANSFER EFFICIENCY e_ε AT H-BAR STRAIN GAUGE H45 (METHOD 2) COMPARED TO 3D FINITE ELEMENT SOLUTIONS (DATA FROM JANUARY/FEBRUARY 1996)

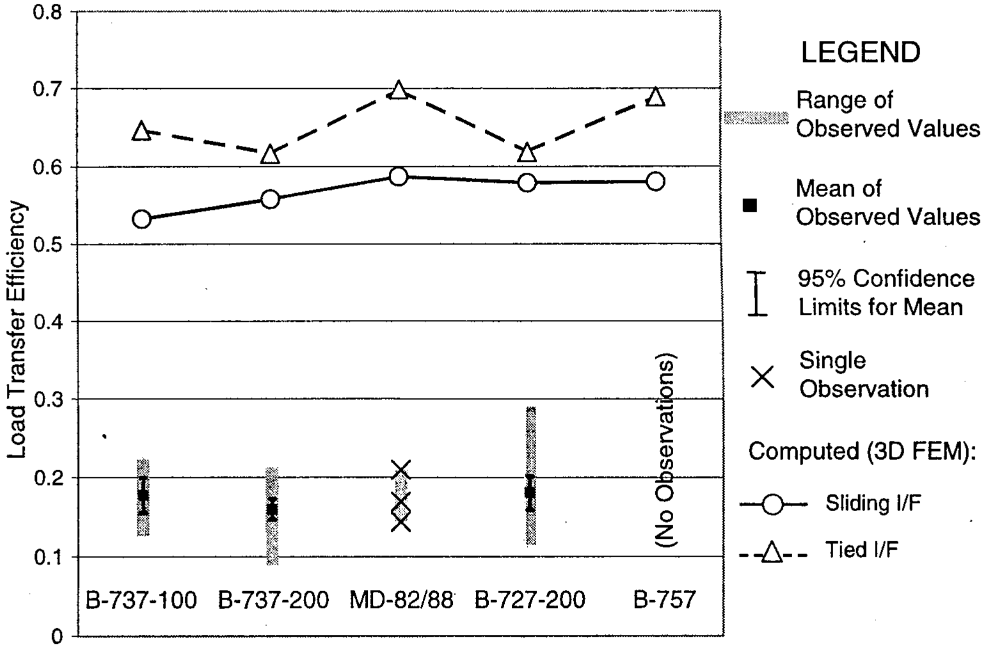

FIGURE 35. STRAIN-BASED LOAD TRANSFER EFFICIENCY e_ε AT H-BAR STRAIN GAUGE H26 (METHOD 2) COMPARED TO 3D FINITE ELEMENT SOLUTIONS (DATA FROM NOVEMBER/DECEMBER 1996)

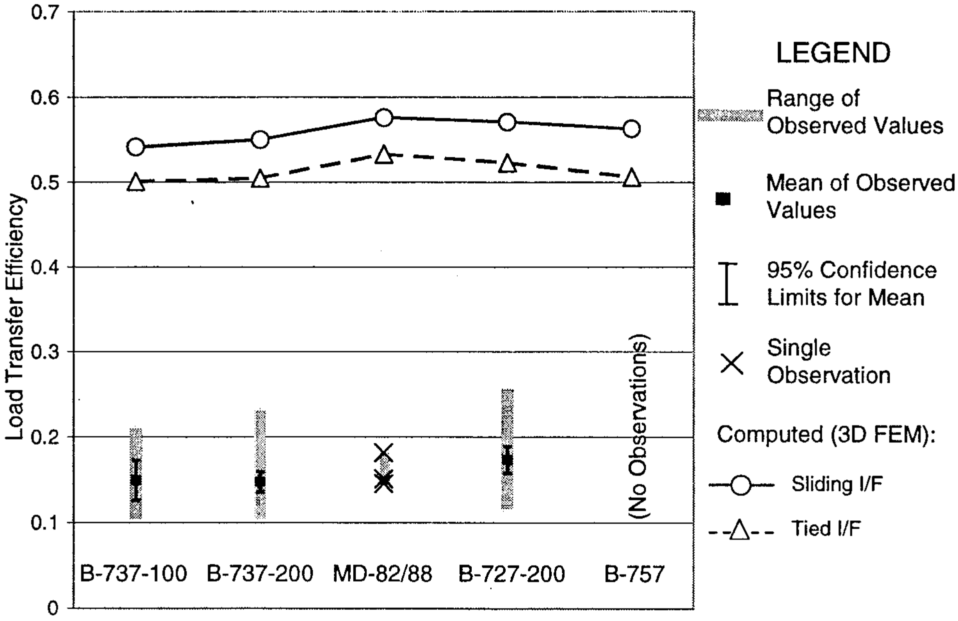

FIGURE 36. STRAIN-BASED LOAD TRANSFER EFFICIENCY e_ε AT H-BAR STRAIN GAUGE H45 (METHOD 2) COMPARED TO 3D FINITE ELEMENT SOLUTIONS (DATA FROM NOVEMBER/DECEMBER 1996)

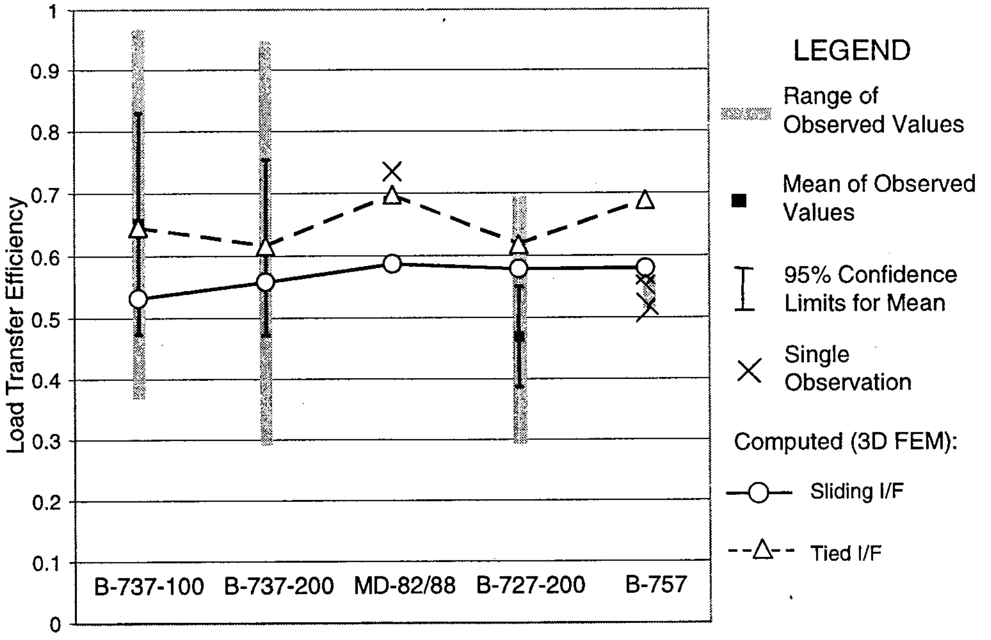

FIGURE 37. STRAIN-BASED LOAD TRANSFER EFFICIENCY e_ε AT H-BAR STRAIN GAUGE H26 (METHOD 2) COMPARED TO 3D FINITE ELEMENT SOLUTIONS (DATA FROM JULY/AUGUST 1997)

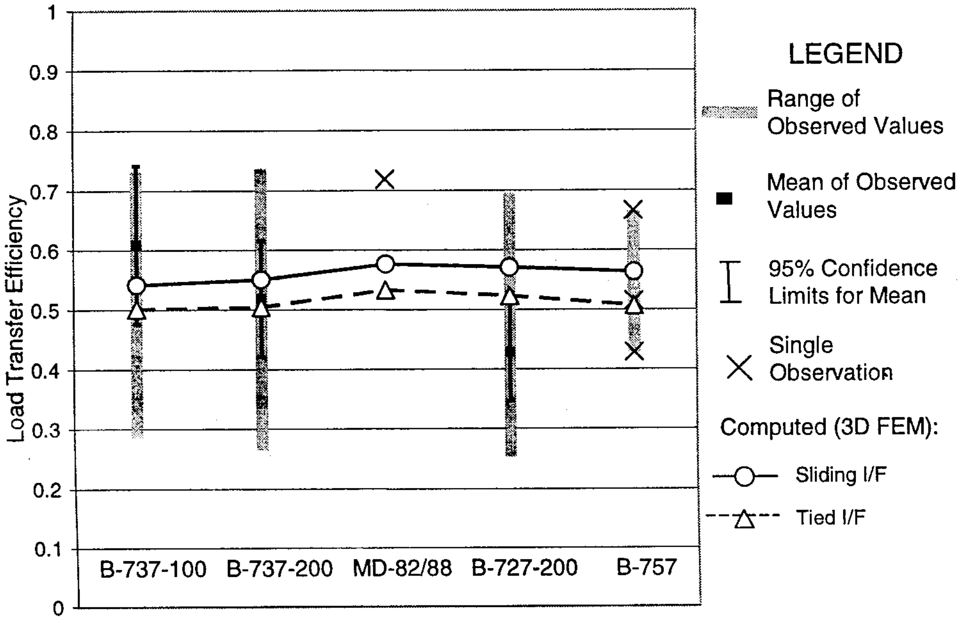

FIGURE 38. STRAIN-BASED LOAD TRANSFER EFFICIENCY e_ε AT H-BAR STRAIN GAUGE H45 (METHOD 2) COMPARED TO 3D FINITE ELEMENT SOLUTIONS (DATA FROM JULY/AUGUST 1997)

From an examination of figures 33 through 38 for the doweled joints, the following observations can be made.

1. Mean in-service load transfer efficiency at the joint was significantly higher during the summer (figures 37 and 38) than during the winter (figures 33 and 34) or fall (figures 35 and 36). From figures 37 and 38, the measured mean load transfer efficiency for summer was in the range 0.5 to 0.7, compared to only 0.25 to 0.35 in figures 33 through 36. This large difference is somewhat unexpected since, in theory, the dowel bars should limit the seasonal variation of load transfer efficiency. The fact that measured mean load transfer efficiency of the doweled joints at DIA was much lower in the winter than in the summer suggests that the dowel bars are not performing as intended and that much of the observed load transfer is attributable to aggregate interlock or other seasonally sensitive mechanisms rather than shear transfer through the bars.

2. In general, the mean strain-based load transfer efficiencies based on the readings at the bottom of the PCC slab (H26) were higher than those based on the readings at the top of the slab (H45).

3. The computed values of load transfer efficiency are comparable to the mean measured values for the summer time period (figures 37 and 38) but are much higher than the corresponding values for the winter and fall time periods (figures 33 through 36).

4. With two exceptions, the mean values of in-service strain-based load transfer efficiency were not significantly affected by the loading aircraft type. The two exceptions are shown in figure 33 (where the B-727-200 mean value is significantly higher than the mean values for the B-737-100 and B-737-200 (based on a 5% threshold for statistical significance)) and figure 34 (where the B-727-200 and B-757 mean values are significantly higher than the B-737-100 and B-737-200 values). In all other cases, there are no statistically significant differences among the observed means at the 5% level.

5. The computed values of load transfer efficiency are not significantly affected by the loading aircraft type.

6. When the fully bonded interface was assumed in the 3D finite element model, this resulted in computed values of load transfer efficiency at the bottom of the slab (H26) that were as much as 10% higher than the corresponding values for the fully unbonded case. However, the values computed at the top of the slab (H45) were approximately 5% lower.

SUMMARY AND CONCLUSIONS

A 3D finite element computer model developed by the FAA computes structural responses of rigid airport pavements to complex aircraft gear loads. Numerical predictions of the 3D finite element model were compared to field data obtained from the FAA instrumented runway located at DIA. Comparisons were performed for a variety of aircraft gear types and for both interior and edge-of-slab loads.

A large amount of variation was observed in the measured pavement responses for aircraft within a given type, even after the measured responses had been adjusted to account for the unavoidable variation in the weights of the loading aircraft. Because of the high variability in the readings, comparison of 3D finite element results with individual sensor readings (as opposed to aggregate values) may give misleading results. Therefore, standard statistical methods were used to analyze the collected raw data and to obtain mean values of key responses (with 95% confidence limits) that were then used for comparison to numerical results. Specific responses studied were peak strain, peak deflection, and load transfer efficiency at transverse joints.

Two methods of estimating in-service load transfer efficiency of transverse joints (based on either strain or deflection ratios) from dynamic sensor records were developed. The first method requires simultaneous readings from sensors located on two opposite sides of the joint. The alternative method needs only one sensor, but involves subjective geometric interpretation of the sensor record. However, the correlation between the two methods is extremely good.

Major findings from the DIA comparisons are as follows.

1. Computed concrete strains from the 3D finite element model were in very good agreement with mean values of peak strain recorded by dynamic strain gauges at the DIA site.

2. Computed tensile strains in the concrete slab are strongly dependent on the type of bond assumed for the horizontal interface between the bottom surface of the slab and the top surface of the base layer. In general, if no bond was assumed for the interface (bond breaker conditions), the 3D finite element model over predicted the magnitude of the mean peak tensile strain in comparison with strain gauge readings. On the other hand, when a fully developed bond was assumed, the finite element model usually under predicted the mean peak strain magnitude. In some cases, the full bond model predicted the mean peak strain value from sensor readings nearly exactly. This result suggests that, while a fully unbonded model is conservative and is used in practice for design of new rigid pavements, an intermediate bond model may be more realistic.

3. From statistical analysis of the H-bar strain gauge readings for a 20-month period, no evidence was found to support the hypothesized trend, due to reduced joint efficiency, toward higher peak strain readings at slab edges during colder winter months. However, this conclusion could change eventually based on additional data analysis.

4. Computed vertical deflections of the pavement surface from the 3D finite element model were in good agreement with mean values of peak vertical deflection recorded by dynamic deflection transducers (LVDTs) at the DIA site. The computed deflections were based on a finite element mesh with a rigid boundary at a 10-foot (3.05-m) depth, corresponding approximately to the anchor depth of LVDT sensors installed at the site.

5. Significantly less variation was associated with the LVDT readings at the interior slab location than at locations near joints. This phenomenon was attributed to the greater exposure of the slab edge to environmental factors, particularly to temperature fluctuations that affect the load transfer capability of the joint.

6. Peak deflection readings at the slab edge are affected significantly by seasonal temperature changes. Analysis of data from one LVDT (SDD17) found a medium-to-strong negative correlation between peak deflection values and the concrete surface temperature recorded at the time of events.

7. Deflection-based load transfer efficiency values evaluated from field data for a dummy contraction joint tended to range from very low (less than 10%) to very high (greater than 90%) for the same aircraft depending on environmental conditions. Different load transfer efficiency regimes were observed depending on whether events occurred in the summer or winter months. ANOVA performed on the DIA data revealed statistically significant differences in the load transfer efficiency response for different aircraft groups for the winter data, but not for the summer data. By contrast, the deflection-based load transfer efficiency values obtained from 3D finite element analysis were in excess of 90% for all the aircraft groups, with no significant variation based on aircraft type.

8. Strain-based load transfer efficiency values were evaluated from DIA data for two different transverse joints: (a) a dummy contraction joint and (b) a doweled joint. Again, there were significant variations in the mean load transfer efficiency based on the season, with much higher values observed in the summer. Comparisons with 3D finite element results showed good agreement between the computed values of load transfer efficiency and the DIA mean values based on summer data. Neither the computed values nor the mean values based on DIA data were strongly affected by the loading aircraft type.

9. Finite element results for the dummy joint are based on an assumed value of the joint spring stiffness (equal to 100,000 lb/in^2 (690 MPa)). The use of a higher spring stiffness to represent the doweled joint resulted in relatively small increases in the computed value of strain-based load transfer efficiency.

REFERENCES

1. Brill, David R., "Development of Advanced Computational Models for Airport Pavement Design," Report No. DOT/FAA/AR-97/47, U.S. Dept. of Transportation, Federal Aviation Administration, Office of Aviation Research, Washington, DC, August 1998.

2. Lee, X., Hovan, M., King, R., Dong, M., and Hayhoe, G.F., "Runway Instrumentation at Denver International Airport: Development of Database," in Aircraft/Pavement Technology – In the Midst of Change, Proceedings of the 1997 Airfield Pavement Conference, Seattle, Washington, F.V. Hermann, editor, ASCE, 1997.

3. Dong, M., Hayhoe, G.F., and Fang, Y.W., "Runway Instrumentation at Denver International Airport: Dynamic Sensor Data Processing," in Aircraft/Pavement Technology – In the Midst of Change, Proceedings of the 1997 Airfield Pavement Conference, Seattle, Washington, F.V. Hermann, editor, ASCE, 1997.

4. Denver International Airport Preliminary Pavement Design Report, Isbill Associates, Inc., Aurora, Colorado. Revision 1, July 15, 1991.

5. Ioannides, A.M. and Korovesis, G.T., "Analysis and Design of Doweled Slab-on-Grade Pavement Systems," Journal of Transportation Engineering, Vol. 118, No. 6, ASCE, 1992.

6. Brill, D.R. and Guo, E.H., "Load Transfer in Rigid Airport Pavement Joints," Proceedings of the International Air Transportation Conference 2000, San Francisco, ASCE, June 2000.

7. Hammons, Michael I. and Freeman, Reed B., "Finite Element Modeling for Rigid Pavement Joints, Advanced Pavement Design: Report 3: Model Simplification and Application," U.S. Dept. of Transportation, Federal Aviation Administration, Office of Aviation Research, Washington, DC, (draft report, in publication).

8. Hammons, Michael I. and Ioannides, Anastasios M., "Finite Element Modeling for Rigid Pavement Joints, Advanced Pavement Design: Report 1: Background Investigation," Report No. DOT/FAA/AR/CT-95/85, U.S. Dept. of Transportation, Federal Aviation Administration, Office of Aviation Research, Washington, DC, April, 1997.

9. Rollings, Raymond S., "Design of Overlays for Rigid Airport Pavements," Report No. DOT/FAA/PM-87/19, U.S. Department of Transportation, Federal Aviation Administration, April 1988.